Title
MODEL OF POSITIVE ION SOURCES FOR MFE NEUTRAL BEAM INJECTION

Authors
Chan, C.F.
Burrell, C.F.
Cooper, W.S.

Publication Date
1983-02-01

Lawrence Berkeley Laboratory
UNIVERSITY OF CALIFORNIA

Accelerator & Fusion Research Division

Submitted to the Journal of Applied Physics

MODEL OF POSITIVE ION SOURCES FOR MFE NEUTRAL BEAM INJECTION

Chun Fai Chan, C.F. Burrell, and William S. Cooper

February 1983

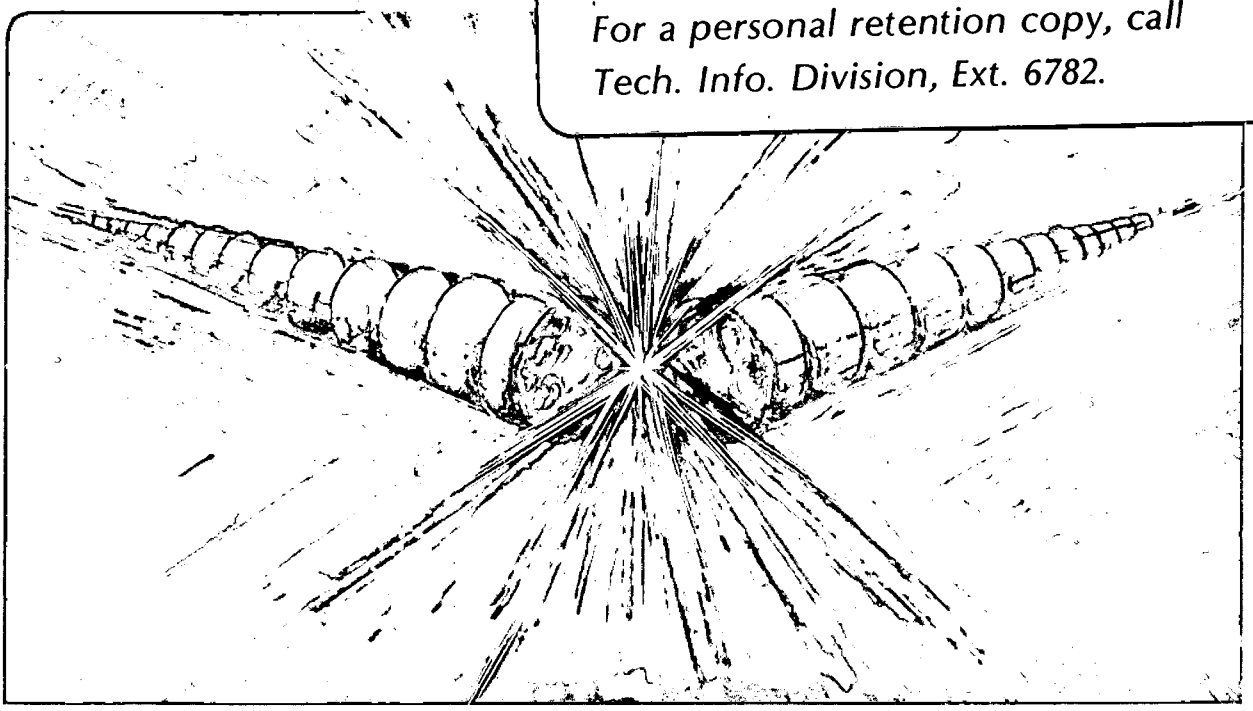

Prepared for the U.S. Department of Energy under Contract DE-AC03-76SF00098

DISCLAIMER

Model of Positive Ion Sources for MFE Neutral Beam Injection*

Chun Fai Chan, C. F. Burrell, William S. Cooper

Lawrence Berkeley Laboratory
University of California
Berkeley, CA 94720

ABSTRACT

A comprehensive model is presented to describe the physics of positive ion sources used to generate hydrogen isotope neutral beams for the heating of confined plasma in magnetic fusion energy programs. The model considers eleven important atomic and molecular reactions. A set of particle balance equations, together with those for the primary and secondary electrons in the sources, are solved simultaneously. Taking as input the source geometry, gas inlet flow rate, arc current and voltage, as well as the wall recombination coefficient and the measured temperatures of neutral atoms and molecules, the model gives as output the following information: the ion current densities available for extraction, primary electron density and energy distribution, and secondary electron density and temperature. These calculated results are compared with data of several LBL ion sources, both conventional and magnetic bucket types. Exploratory calculations are made for sources of different proposed designs with the aim of improving the source performance.

---

* This work was supported by the Director, Office of Energy Research, Office of Fusion Energy, Applied Plasma Physics Division, of the U. S. Department of Energy under Contract No. DE-AC03-76SF00098.

I. INTRODUCTION

The most successful method of heating magnetically confined plasma to thermonuclear temperatures at present consists of the injection and capture of energetic neutral hydrogen isotopes.[1] The injected particles transverse the external magnetic field unhindered and become trapped in the confinement region by charge exchange and ionizing collisions, and their energy is then shared with the target plasma by Coulumb collisions.

To make the neutral beam, ions are produced in an ion source, accelerated to the desired energy, and then converted into neutrals by charge-exchange collisions in a gas cell. The ion source is the subject of this paper. Using deuterium as an example, the positive ion source produces not only D_1^+ ions but also D_2^+ and D_3^+ ions. We shall pursue by analytical and numerical means a better understanding of the physics involved, hoping thereby to gain some insight into the trend of the experimental results, and be able to improve the performance characteristics of the source. For example, it may be very desirable to maximize the D_1^+ fraction output of the ion source. The reason is that the accompanying D_2^+, D_3^+ ions, which are also accelerated, break up in the neutralizer and produce components in the neutral beam at 1/2 and 1/3 of the full energy, which are undesirable or even harmful for many applications. In other cases, it may be desirable to maximize the output of one of the molecular ions. Other questions can also be addressed, such as gas efficiency, electrical power efficiency, etc.

An earlier work in developing a systematic source model was done by the British Culham Group[2], followed in essentially identical ways by

other authors in Russia[3] and Japan[4]. In developing our source model[5] we have benefitted greatly from the work of Ref. 2, but our work differs from that of the Culham group substantially in several features, which we think are improvements. Let us just point out a few of them here briefly, leaving the technical details in Sect.II.C.

1. We have computed more accurately the rate coefficients involving 11 important reactions of hydrogen species.
2. The temperatures of neutral atomic and molecular gas have been measured experimentally, and are treated as known quantities in the model.
3. The boundary condition involving neutral molecular gas density is related to the gas feed flow rate, which is readily measurable.
4. In addition to the five particle balance equations for species D_1, D_2, D_1^+, D_2^+, D_3^+, there are also particle and energy balance equations for the secondary electrons, which are used to calculate their density and temperature, with the help of the charge neutrality condition.
5. We calculate the energy distribution of the primary electrons self-consistently. Primary electrons, with initial energy equal to the arc voltage, lose their energy by various inelastic reactions. The process is then repeated until their energies fall below the lowest reaction threshold, or they are lost to the wall.

With these ingredients we then proceed to construct the model. Because of the complexity of the reactions involved and the number of

hardware components in the sources, it is almost unavoidable that a simple model shall have some phenomenological aspects. However, in a pragmatic way we shall develop a tool that, with minimal amount of input information, can explain existing data with reasonable accuracy and have some predictive prowess to project the results of other source operating regimes or of sources of different designs. These are reported in Sections II, III and IV below. Further possible improvements and applications of the model are discussed in Section V.

We also would like to mention here that the primary electron energy degradation scheme we use in this paper has some similarity with those used by some authors[6] in other gas systems, such as the works on computer modeling of gas lasers, and on upper atomspheric research.

II. THE MODEL

A. Preliminary

We begin by giving a brief review of the concept of the particle balance equation. This also serves to introduce notations.

Consider the case of a box containing ions created by the collisions of electrons with neutrals. In steady state, in a volume of plasma, the rate of ion-creation must equal the rate of ions escaping through the surface enclosing that volume;

$$\int dV\ S\ n_e\ N_o = \int dA\ n_i\ v_i, \tag{1}$$

where $S = \langle \sigma v_e \rangle$ is the collision rate coefficient, n_e, N_o and n_i are the densities of electrons, neutrals and ions respectively, and v_i is the velocity of the ion. If the plasma is isotropic and we consider no spatial variation of N_o for the moment (some correction for an anisotropic situation will be discussed later), then

$$VS\ \bar{n}_e N_o = A\ n_i\ v_i, \tag{2}$$

where

$$\bar{n}_e = \frac{1}{V} \int d\,V\ n_e\ . \tag{3}$$

Notice that in Eq. (2), $\bar{n}_e$ refers to the quantity inside the volume, whereas n_i and v_i refer to quantities at the enclosing surface, the plasma boundary. Now in general there is a plasma-sheath structure. On

the right hand side of Eq. (2), n_i decreases and v_i increases rapidly in the sheath region as the ions move toward the wall. The potential also drops dramatically in the sheath region. However, the ion current density stays nearly constant because most of the ions are created in the plasma region where the electron density is large. How should we choose n_i then in our particle-balance equation?

We will argue that, to a good approximation, a well-defined choice can be made for n_i and v_i. Let us illustrate this with a one-dimensional model due to Tonks and Langmuir[7], as analyzed by Self[8]. Consider the ion current density (flux) at the wall with coordinate $z = z_w$,

$$J_i(z_w) = n_i(z_w)\ v_i(z_w) \tag{4}$$

$$= \int_0^{z_w} dz\ S\ n_e\ N_o \tag{5}$$

$$= z_w\ S\ N_o\ \frac{1}{z_w} \int_0^{z_w} dz\ n_e \tag{6}$$

$$= z_w\ S\ N_o\ \bar{n}_e \tag{7}$$

$$= z_w\ S\ N_o\ \bar{n}_i, \tag{8}$$

where in the last step we use the charge neutrality requirement

$$\bar{n}_e = \bar{n}_i. \tag{9}$$

Therefore, Eq. (4) can be rewritten as

$$j_i(z_w) = \bar{n}_i \, \bar{v}_i , \tag{10}$$

where $\bar{n}_i$, just like $\bar{n}_e$ in Eq. (3), is the volume-averaged density, and $\bar{v}_i \equiv z_w \, S \, N_o$.

Now z_w can be decomposed[8] as

$$z_w = s_w \cdot \frac{1}{S \, N_o} \left(\frac{2kT_e}{m_i} \right)^{1/2} , \tag{11}$$

where s_w is the "reduced" wall distance, a dimensionless number, kT_e is the electron temperature, and m_i is the ion mass. The important feature about this particular decomposition (or scaling) is that s_w, as Self[8] demonstrated in his numerical result, depends only weakly on the parameters of the plasma or the geometry. In the range of plasma parameters that concerns us in this ion source study, s_w stays nearly constant with a value $s_w \approx .43$. Therefore, we can define a volume averaged velocity

$$\bar{v}_i = s_w \left(\frac{2kT_e}{m_i} \right)^{1/2} . \tag{12}$$

This, together with $\bar{n}_i$ defined similarly to $\bar{n}_e$ in Eq. (3), gives us Eq. (10). There are two advantages to this approach:

1. Equation (10) is essentially position-independent in the sheath

region. This relieves us from choosing an artificial plasma-sheath boundary.

2. In a particle balance equation, such as Eq. (2), every density is volume-averaged. In case a particle species appears on both sides of the equation, it refers to the same volume-averaged quantity. (Note: we are aware that in general $\bar{n}_1 \cdot \bar{n}_2 \neq \overline{n_1 n_2}$. We have studied the case where the densities have parabolic shapes, and found the two sides differ by about 10%; we shall ignore this complication.) In practical computation for the cases given below, with varying electron temperature and neutral density, etc., s_w is kept constant. Overall good agreement between computer results and data are obtained with a value of 0.43 for s_w as given by Self.[8]

From Eq. (12) we define an average ion lifetime

$$\bar{\tau}_i = \frac{V}{A} \frac{1}{\bar{v}_i} \quad . \tag{13}$$

Therefore Eq. (2) can be rewritten as

$$\bar{n}_e N_o S = \bar{n}_i / \bar{\tau}_i . \tag{14}$$

Beginning in the next Section, the bar which stands for volume-averaging will be omitted for simplicity of notation.

B. Physical Assumptions of the Model

The plasma that concerns us is contained in an ion source as sketched in Fig. 1. Basically, the device is a cylindrical or rectangular box with filaments and a gas inlet for D_2 or H_2 in the back, and a gridded opening for extraction of the produced ions in the front. The filaments inject primary electrons to produce the discharge and serve as cathode, while part or all of the side and back walls serve as anode. These walls may have permanent magnets outside them to improve the confinement of charged particles. The front wall is either electrically floating, or is connected to the negative end of the filaments. Detail hardware structures of various sources can be found in references cited in Section IV.

The gas usually used for MFE application is D_2, but in the following paragraphs we shall sometimes also talk about H_2 gas, since its basic physical data are readily available. It is understood that any isotope effect for D_2 gas can be taken into account.

For the construction of the model to describe the performance of the ion source, we shall make the following physical assumptions or taken as empirical facts:

1. The Reactions: we include 11 reactions involving hydrogen species in the plasma volume. A list of these reactions and other related information follows:

	REACTIONS	RATE COEFF.	E_r (DATA)	E_r(THEORY)
1.	$H + e \rightarrow H^+ + 2e$	S_1	13.9	13.6
2.	$H_2 + e \rightarrow 2H + e$	S_2	9.2	10.6
3.	$H_2 + e \rightarrow H_2^+ + 2e$	S_3	16.0	15.6
4.	$H_2^+ + e \rightarrow 2H$	S_4	0.33	0.0
5.	$H_2^+ + e \rightarrow H^+ + H + e$	S_5	3.45	12.1
6.	$H_2^+ + H_2 \rightarrow H_3^+ + H$	S_6	0.01	0.0
7.	$H_3^+ + e \rightarrow H^+ + H_2 + e$	S_7	15.0	15.0
8.	$H_3^+ + e \rightarrow H_2 + H$	S_8	0.38	0.0
9.	$H + e \rightarrow H(2s, 2p) + e$	Q_1	10.0	10.2
10.	$H_2 + e \rightarrow H_2(B,C,D) + e$	Q_2	20.0	12.0
11.	$H_2 + e \rightarrow H_2(v=1) + e$	Q_3	1.5	2.0

The data of reaction cross-sections are taken from a standard reference[9] as well as from recent journal articles. They all have values of $\sigma > 10^{-17}$ cm^2 somewhere in the energy region of interest. We have also computed the reaction rate coefficients. In Fig. 2A and 2B we plot $\sigma.v$ vs E, the energy of the primary electron, except for Reaction No. 6 where E stands for the energy of the incident H_2^+ in the laboratory frame. In Fig. 3A and 3B, we plot $\langle\sigma.v\rangle$ vs kT_e, the temperature of the Maxwellian electrons. Some remarks about these reactions and cross section values are given in Appendix A.

In the list above E_r stands for the threshold energy for each reaction. The E_r(data) means the lowest energy listed in reference articles, whereas E_r(theory) is the theoretical energy threshold. In the case of molecular reactions, the energy is computed for the lowest Frank-Condon transition. Usually these two values are quite close

together except for the case of reaction No. 5, in which highly excited vibrational states in some experiments may make the transition to an unbound state much easier. Fortunately, as we see in Fig. 2A, the $\sigma.v$ value in this case is quite insensitive to E.

2. Ion Velocities: We assume that the ions, once produced, are accelerated to the sides, and we shall use the volume-averaged velocity introduced above for each of them. Some of the H_2^+, and H_3^+ ions, however, may be dissociated before they reach the walls. As far as averaged velocity is concerned, we ignore the difference between those H_1^+ coming from the ionization of H_1 and those coming from the dissociations of H_2^+ and H_3^+. The validity of this "free-fall" assumption is of course contingent on the condition that the neutral gas densities are not too high. Careful Langmuir probe measurements,[10] in a LBL 10-Amp Ion Source, of the spatial dependence of plasma potential, plasma density and saturated ion current density show the behavior typical of the free-fall model prediction. The characteristic lengths, defined as the volume - to - surface ratios of the sources (as can be seen from Eq. (13)) which have values in the range 2 to 4 cm for the cases studied, are smaller than estimates of the ion-neutral elastic or charge exchange mean free paths.

E. K. Shaw[11] used the fluid equations to study the correction to the free-fall model due to ion-neutral collisions. For example, one can show from his result that in a one-dimensional planar model, for the case when the ion-neutral collision frequency equals to electron-neutral ionization frequency, (this corresponds to about the worst situation in our sources,) the potential, charge densities and current densities at

the sheath edge, differ by only about 10% from those calculated from pure free-fall model. The resulting potential profile is somewhat steeper than in the collisionless case; this reduces the electron current and enhances the ion current leaving the plasma.

3. Neutral Temperatures: The ions escape with an energy of several eV, set by the electron temperature, and they pick up most of this energy during their transit through the sheath to the wall. Implicit in this assumption is that their initial velocities are ignored. We can ignore the initial velocity contribution from the parent neutrals because we know that they have temperatures of only a fraction of 1 eV. We have done a set of systematic measurements of the temperature of the neutral species in the sources. The results are given in Appendix B. In our calculation we have set the temperature of the neutral atoms $kT_1 \sim 0.35$ eV and the temperature of the neutral molecules $kT_2 \sim 0.12$ eV, which are consistent with the measurements in the 10-amp conventional source at medium arc power. The measured temperatures show little dependence on gas flow and little isotope effect; however, they do show some dependence on arc power which we neglect in our calculations. The reasons for these temperatures (as compared with the room temperature $kT_2 \sim 0.025$ eV) are rather complicated, and are no doubt related to the dissociation energy of the molecules, exchange of energy between particles and the walls, etc. Since they are nearly constant we shall be content to treat them as empirical input parameters in our model.

4. Wall Recombination Coefficient of H_1: The transformations of atoms to molecules can be attributed almost entirely to surface recombinations on the walls of the source, since the volume recombination

cross section is very small. Wood and Wise[12] measured the recombination coefficients γ of H_1 on various surfaces; γ is defined as the ratio of atoms that strike the surface and recombine forming molecules to the total number colliding with the surface (i.e., $\gamma = 1 - f_{out}/f_{in}$, where f is the neutral atomic flux). They found $\gamma = 0.1$ to 0.25 for most metal surfaces. For example, measured values of γ as a function of the temperature of the metal surface are, for tungsten:

$T(^oK)$ =	353	423	533	563	578	643	678	723	923	1088
γ_W =	0.065	.055	.068	.052	.054	.059	.062	.057	.062	.067

and, for copper:

$T(^oK)$ =	333	543	693
γ_{Cu} =	0.14	.10	.10

These data show that the value of γ is insensitive to the surface temperature in the ranges of measurements. In our sources the walls are made of stainless steel or copper contaminated by the deposition of tungsten evaporated from the filaments. For the source model, we treat γ as a constant parameter; we found we needed $\gamma \sim 0.2$ for D_1 to explain the measured data.

As to the possibility of the conversion of ions into neutral molecules at the walls, it is of little consequence since the flux of ions is one or two orders of magnitudes smaller than the neutral H_1 flux. We have studied the case where each proton reacts with the wall just like a neutral atom and found that computed results are changed by only a few percent.

C. The Equations

1. Particle Balance Equations

Based on the physical assumptions stated above, plus the requirements of the conservation of nuclear flux and charge neutrality of the plasma, we have

$$n_1: \quad N_1 n_e S_1 + n_2 n_e S_5 + n_3 n_e S_7 = n_1/\tau_1 \tag{15}$$

$$n_2: \quad N_2 n_e S_3 = n_2 n_e (S_5 + S_4) + N_2 n_2 S_6 + n_2/\tau_2 \tag{16}$$

$$n_3: \quad N_2 n_2 S_6 = n_3 n_e (S_7 + S_8) + n_3/\tau_3 \tag{17}$$

$$N_1: \quad 2N_2\, n_e S_2 + n_2 n_e (S_5 + 2S_4) + n_3 n_e S_8 + N_2 n_2 S_6 = N_1 (n_e S_1 + \gamma/T_1) \tag{18}$$

$$N_2: \quad (n_1 v_1 + 2\, n_2 v_2 + 3 n_3 v_3) A_I + (N_1 v_{01z} + 2 N_2 v_{02z}) A_0 = 2F \tag{19}$$

$$n_e: \quad n_1 + n_2 + n_3 = n_e \quad . \tag{20}$$

The meanings of most of the symbols are obvious; they are defined similarly to those in Section II.A and B above. Densities and velocities are volume-averaged. The meanings of other symbols in these equations follow:

$$v_{01z} = \frac{1}{4} v_{01} = \frac{1}{4} \left(\frac{8}{\pi} \frac{kT_1}{m_1} \right)^{1/2} , \tag{21}$$

$$v_{02z} = \frac{1}{4} v_{02} = \frac{1}{4} \left(\frac{8}{\pi} \frac{kT_2}{m_2} \right)^{1/2} , \tag{22}$$

$$T_1 = \frac{V}{A}\frac{4}{v_{01}} \quad , \tag{23}$$

A_0, A_I = loss areas for neutrals, ions, (24)

F = input H_2 flow rate, 1 Torr-L/sec = 3.54×10^{19} molec./sec. (25)

We assume the electron population consists of a Maxwellian distribution (secondaries) plus groups of primaries with different energies, so actually (see Sect.II.C.2 below)

$$n_e S \gg n_e S + \sum_g n_{pg} S'_g \quad . \tag{26}$$

We have three additional remarks:

i) Some aspects of the anisotropy of the flux of ions leaving the plasma body can be taken into account as follows. If the ions free-fall to the negative wall but reach the anode by inherently random motion (that is, if the plasma potential equals the anode potential), then we can define

$$\tau_i = \frac{V}{A_w v_i + A_a v_{ia}} \quad , \tag{27}$$

where v_i is given by Eq. (12), and

$$v_{ia} = \frac{1}{4}\left(\frac{8}{\pi}\frac{kT_i}{m_i}\right)^{1/2} \quad . \tag{28}$$

For our plasma we have $kT_i \lesssim 1$ eV.

ii) Implicit in Eq. (15) to Eq. (19) is the assumption that all ions turn into neutral molecules when they hit the walls. If instead of this

we assume that each proton or deuteron has a certain probability of returning as a neutral atom, then we should add the following to the left hand side of Eq. (18):

$$(1-\gamma_1)\, n_1/\tau_1 + (1-\gamma_2)2n_2/\tau_2 + (1 - \gamma_3)3n_3/\tau_3 \qquad (29)$$

with no change to other equations. In Eq. (29), the γ_i's are defined similarly to the γ's for neutral atoms in Sect.II.B.4. A reasonable choice would be $\gamma_1 = \gamma_2 = \gamma_3 = \gamma$, in view of the lack of experimental information about any of them. In the application of the model, we found that this choice gives a few percent more of n_1 in comparison with the original version of the model without the addition of (29). However, a model including (29) and with $\gamma = 0.3$ gives an almost identical result to a model without (29) but using $\gamma = 0.2$. In view of the uncertainties mentioned above, we will use the simpler version.

iii) There is another technical complication concerning the extraction areas for neutrals and ions. Immediately outside the exit area of the source (Fig. 1) is a duct containing sets of electrodes for accelerating and focusing the ion beam. The duct serves as a gas cell for converting the ion beam into a neutral beam. An ion that hits the opening area A_I of the source will thus have a very high probability of escape, but a neutral can backscatter from the accelerator electrode structure or the duct walls and return to the source. We have conducted two studies, one by an

analytical model, and one by Monte Carlo calculation, to find out the effect of this neutral backflow. We found out that for a typical structure, including the duct, there is about a 25% probability that a neutral , once it leaves the source, will escape completely and not return. Hence we set

$$A_O = \frac{1}{4} A_I \tag{30}$$

The choice of this transmission probability is obviously geometry - and application - dependent. Fortunately, model results do not depend sensitively on the value of this parameter, since a change in the transmission probability can be compensated for by a change in gas flow into the source. It should also be noted that Eq. (30) has a bearing on the gas efficiency of the source operation.

2. Primary Electrons

The primary electrons, emitted from the hot filaments in the source, have an initial energy determined by the arc voltage, which is typically 60 volts. (We ignore the energy spread due to the small potential drop along the filaments. From temperature distribution measurements it has been concluded[13] that the majority of the electrons are emitted from the negative legs of the filaments.) In the model, these primaries then participate in all the various reactions listed above. After the first interaction, reactions numbers 1,2,3,5,7,9,10 give rise to another "generation" of primaries with energies diminished by an amount appropriate for each reaction, 10-20 eV. These degraded primaries are still quite energetic and in general have large $S' = \sigma.v$, as can be seen from Fig. 2A-2B. This process continues until their energies fall below the lowest E_r, i.e., E_{rmin} among the seven reactions mentioned above, or they are lost by dissociative recombination with ions or to the wall. The population of each generation is governed by the following set of equations:

a. First Generation: $E_1 = eV_{arc}$; 1 equation:

$$I_p = \frac{1}{4} n_{p1} v_{p1} A_{p1} + n_{p1} (\sum_k S_n' N_n + \sum_k Q_k' N_k) V \quad , \tag{31}$$

$$\therefore n_{p1} = I_p [\frac{1}{4} v_{p1} A_{p1} + (\sum_k S_k' N_k + \sum_k Q_k' N_k) V]^{-1}, \tag{32}$$

where

$$A_{p1} = A_{anode} + A_{wall} (1 + \frac{\phi_{wall}}{E_1}) \quad , \tag{33}$$

$$\sum_k S'_k N_k = S'_1 N_1 + (S'_2 + S'_3) N_2 + n_2(S'_5 - S'_4) + n_3(S'_7 - S'_8) \quad , \tag{34}$$

$$\sum_k Q'_k N_k = Q'_1 N_1 + Q'_2 N_2 \quad . \tag{35}$$

b) Second Generation: $E_{2i} = E_1 - \epsilon_i$, $i = 1,\ldots,7$; 7 equations:

$$n_{p1} R'_i N_i . V = \frac{1}{4} n_{p2i} v_{p2i} A_{p2i} + n_{p2i} (\sum_k S'_k N_k + \sum_k Q'_k N_k) V \quad , \tag{36}$$

$$\therefore n_{p2i} = n_{p1} R'_i N_i \; V \left[\frac{1}{4} v_{p2i} A_{p2i} + (\sum_k S'_k N_k + \sum_k Q'_k N_k) V \right]^{-1} \quad , \tag{37}$$

where

$$R'_i N_i = S'_1 N_1, \; S'_2 N_2, \; S'_3 N_2, \; S'_5 n_2, \; S'_7 n_3, \; Q'_1 N_1, \; Q'_2 N_2 \; . \tag{38}$$

c) Third Generation: $E_{3ij} = E_{2i} - \epsilon_j$; 7^2 equations.

d) m^{th} Generation: $E_{mi_1 i_2 \cdots i_{(m-1)}} = E_{(m-1) i_1 i_2 \cdots i_{(m-2)}} - \epsilon_{i_{(m-1)}}$; $7^{(m-1)}$ equations.

Remarks:

i) The primary current $I_p = I_{arc}$ for floating walls; $I = I_{arc} - (j_1 + j_2 + j_3) A_{wall}$ for the case when the wall is tied to the negative end of the filaments. (Here all the I's and j's are fluxes; they can be converted readily into currents or current densities whenever necessary in numerical calculations.)

ii) In Eq. (33), A_{anode} is the effective anode area for the primary electrons. Usually the anode potential is very close to the plasma potential, differing by about 1 volt. The other inside areas of the source chamber, including the filament areas, as denoted by A_{wall}, are electrically negative with respect to the plasma potential. We have assumed that the primary electrons are spatially isotropic.

iii) $\epsilon_i = E_{r1}, E_{r2}, E_{r3}, E_{r5}, E_{r7}, E_{r9}, E_{r10}$.
If the average energies of the ejected secondaries are included, then

$$E_{r1} > E_{r1} + E_{s1}$$

$$E_{r3} > E_{r3} + E_{s2}.$$

From ejected electron distributions we estimated that (see Appendix C) for $E_1 \sim 30$ to 80 eV,

$$E_{s1} \sim E_{s2} \sim 7 \text{ eV}. \tag{39}$$

iv) This "generation" scheme stops whenever the primary electron reaches $E < E_{rmin}$. For example, let us assume that $E_{rmin} = E_{r9}$. If, say $E_{2i} = E_1 - \epsilon_i < E_{r9}$ for all i's listed in Eq. (38), then Eq. (36) becomes

$$n_{p1} R_i' N_i V = \frac{1}{4} n_{p2i} v_{p2i} A_{p2i} \tag{40}$$

and $n_{p3ij} = 0$ and so on. In Eq. (40) we have neglected the recombination loss of primaries due to S_4 and S_8.

v) In the application of the model shown below, we found that the first generation of primaries produces about half the observed ions. Typically we have to go through 5 generations with 2801 equations to calculate the energy distribution of degraded primaries.

3. Secondary Electrons

We assume the secondary plasma electrons can be represented by a Maxwellian distribution; this is consistent with probe measurement of the source plasma.[10] We will use the particle number balance equation and energy balance equation to determine self-consistently the density n_e and temperature kT_e respectively. (More explanation of the method will be given below).

a) Secondary electron number balance

Production processes include

i) Ionization of neutrals by primaries and secondaries, and

ii) Conversion of primaries into secondaries when the energies of the primaries fall below the lowest reaction threshold.

Loss processes include

i) Loss to the anode and the walls, and

ii) Loss due to dissociative recombination reactions

These processes lead to the following particle balance equation:

$$\sum_g n_{pg}(N_1 S'_{1g} + N_2 S'_{3g})\, V + n_e\,(N_1 S_1 + N_2 S_3)\, V$$

$$+ \sum_{k,g} n_{pg}\, N_k S'_{kg}\, V$$

$$E_g - E_{rk} \leq E_{rmin}$$

$$= \frac{1}{4}\, n_e v_e\, [A_a^{eff} + A_w \exp(\phi_w / kT_e)]$$

$$+ n_e(n_2 S_4 + n_3 S_8)\, V \qquad . \qquad (41)$$

b) Secondary electron energy balance

Energy gain for secondary electrons results from

i) Creation of new secondaries by ionizing reactions by both primaries and secondaries,

ii) Direct coulomb heating by primaries, and

iii) Injection of degraded primaries.

Energy loss for secondaries includes

i) Loss to the anode and walls, and

ii) Loss due to ionization, dissociation, recombination and excitation reactions by the secondaries.

These energy gain and loss processes lead to the following energy balance equation:

$$E_{s1} \sum_g n_{pg} N_1 S'_{1g} V + E_{s2} \sum_g n_{pg} N_2 S'_{3g} V$$

$$+ E_{s1}\, n_e N_1 S_1 V + E_{s2}\, n_e N_2 S_3 V$$

$$+ \sum_g E_g^{-1/2}\, n_{pg}\, \Phi(E_{pg}/kT)\, n_e c\, V$$

$$+ \sum_{k,g} E_g\, n_{pg} N_k S'_{kg} V$$

$$E_g - E_{rk} \leq E_{rmin}$$

$$= \frac{1}{4} n_e v_e \left[A_a^{eff}\, 2kT_e + A_w (2kT_e + |\phi_w|) \exp(\phi_w / kT_e) \right]$$

$$+ (E_{s1} + E_{r1})\, n_e N_1 S_1 V + (E_{s2} + E_{r3})\, n_e N_2 S_3 V$$

$$+ E_{r2}\, n_e N_2 S_2 V + E_{r5}\, n_3 n_2 S_5 V + E_{r7}\, n_e n_3 S_7 V$$

$$+ 0.86 kT_e\, n_e n_2 S_4 V + 1.13 kT_e\, n_e n_3 S_8 V$$

$$+ E_{r9}\, n_e N_1 Q_1 V + E_{r10}\, n_e N_2 Q_2 V + E_{r11}\, n_e N_2 Q_3 V \quad . \qquad (42)$$

Further explanation regarding this equation is given in Appendix C.

4. Floating Wall Potential

The floating wall potential is determined by the condition

$$\sum_i j_i = j_e \exp(\phi_w/kT_e) + \sum_g j_{pg}(1 + \phi_w/E_{pg})\theta \tag{43}$$

where $\theta = \theta(\phi_w/E_{pg})$; $\theta(x) = 1$ for $x < 1$, $\theta(x) = 0$ for $x \geq 1$.

a) If the primary electron current dominates:

$$\phi_w \approx - \frac{\sum_g j_{pg}\theta - \sum_i j_i}{\sum_g \frac{j_{pg}}{E_g}\theta} \quad . \tag{44}$$

From this we see that

$$\phi_w \gtrsim - E_1 \qquad \text{if} \quad \sum_g j_{pg} >> \sum_i j_i \quad . \tag{45}$$

b) If the secondary electron current dominates,

$$\phi_w \approx - kT_e \, \mathrm{Ln} \frac{j_e}{\sum_i j_i} \tag{46}$$

$$\approx - kT_e \mathrm{Ln} \left\{ 2\pi^{1/2} s_w \left(\frac{m_e}{m_1}\right)^{1/2} \cdot \frac{1}{n_e} \cdot \left[n_1 + n_2 \left(\frac{m_1}{m_2}\right)^{1/2} + n_3 \left(\frac{m_1}{m_3}\right)^{1/2} \right] \right\}$$

$$\approx - 4.0 \, kT_e \quad . \tag{47}$$

5. Finally, we remark that the particle balance equations Eq. (15-19) can be rewritten in the forms

$$\frac{n_1}{N_2} = \frac{N_1}{N_2} S_1(n_e\tau_1) + \frac{n_2}{N_2} S_5(n_e\tau_1) + \frac{n_3}{N_2} S_7(n_e\tau_1) \tag{48}$$

$$\frac{n_2}{N_2} = \frac{S_3}{S_5 + S_4 + (n_e\tau_2)^{-1} + \frac{N_2}{n_e} S_6} \approx \frac{S_3}{S_5 + S_4 + (n_e\tau_2)^{-1}} \tag{49}$$

$$\frac{n_3}{N_2} = \frac{n_2 N_2}{N_2 n_e} \frac{S_6}{S_7 + S_8 + (n_e\tau_3)^{-1}} \approx n_2 S_6 \tau_3 \tag{50}$$

$$\frac{N_1}{N_2} = \frac{2S_2}{S_1 + \gamma(n_e T_1)^{-1}} + \frac{n_2}{N_2} \frac{S_5 + 2S_4}{S_1 + \gamma(n_e T_1)^{-1}} + \frac{n_3}{N_2} \frac{S_8}{S_1 + \gamma(n_e T_1)^{-1}}$$

$$+ \frac{n_2}{N_2} \frac{N_2}{n_e} \frac{S_6}{S_1 + \gamma(n_e T_1)^{-1}} \tag{51}$$

$$\frac{2F}{N_2} = \frac{N_1}{N_2} v_{01z} A_0 + 2v_{02z} A_0 + \frac{n_1}{N_2} v_1 A_I + 2\frac{n_2}{N_2} v_2 A_I + 3 \frac{n_3}{N_2} v_3 A_I \quad . \tag{52}$$

Normalized in this form, the particle balance equations are more convenient for computation.

III. GENERAL DISCUSSION OF THE SYSTEM OF EQUATIONS

A. The Total Ion Currents

If we add up Eq. (15) to Eq. (17) we obtain

$$I_i = \sum_i j_i A_i = (N_1 n_e \tilde{S}_1 + N_2 n_e \tilde{S}_3)\, V - (n_2 n_e \tilde{S}_4 + n_3 n_e \tilde{S}_8)\, V \qquad (53)$$

or,

$$I_i \approx (N_1 n_e \tilde{S}_1 + N_2 n_e \tilde{S}_3)\, V \,, \qquad (54)$$

where $n_e \tilde{S}_1 \equiv n_e S_1 + \sum_g n_{pg} S'_g$ as in Eq. (26). Notice that Eq.(54) follows from Eq. (53) because usually the loss of ions due to volume recombinations is much smaller than the production of ions by primary and secondary electrons.

B. The Total Primary Electron Currents

If we add up Eq. (31), Eq. (36), Eq. (40) and so on, we obtain

$$I_p = \sum_{\substack{g \\ E_g > E_{rmin}}} j_{pg} A_{pg} + \sum_{\substack{g \\ E_g \leq E_{rmin}}} j_{pg} A_{pg} \,. \qquad (55)$$

Note that

$$\sum_{\substack{k,g \\ E_g - E_{rk} \leq E_{rmin}}} n_{pg} N_k S'_{kg} V = \sum_{\substack{g \\ E_g \leq E_{rmin}}} j_{pg} A_{pg} \qquad (56)$$

is the total current of primaries degraded into secondaries, which is expected to be considerable smaller than the primary current due to the first term in Eq. (55).

C. The Secondary Electron Current

With the help of Eq. (53) and Eq. (56), Eq. (41) can be

rewritten as

$$I_e = \frac{1}{4} n_e v_e A_e = \sum_i j_i A_i + \sum_{\substack{g \\ E_g \leq E_{rmin}}} j_{pg} A_{pg} \quad . \tag{57}$$

The choice to include those degraded primaries with energies less than E_{rmin} as secondaries is somewhat artificial. We have ignored the fine steps as how these electrons blend in with the Maxwellian body. Presumably this is a good approximation if their population is small in comparison with that of other electrons and E_{rmin} is not too much bigger than kT_e, (recall $E_{rmin} \sim 10$ eV, $kT_e \sim 4$ eV for the plasma in question).

In Eq. (57) the electron loss area A_e consists of two parts, as shown in Eq. (41). The part due to floating or negatively biased walls (and filament areas) is very small due to the exponential factor. The dominant part A_a^{eff} is the effective anode area. It contains implicitly the effect due to the slight difference between the anode potential, which is defined to be zero, and the plasma potential, which usually is zero also, or one to two volts positive. This plasma potential has little effect on the loss of primaries because they are energetic, or on the loss of ions because A_i is dominated by the negative walls A_w (see, however, more discussion on the effect of a negative plasma potential on ion loss later on), but it can reduce the lose of secondaries by a factor of, say, $\exp(-2/4) = 0.61$, for $kT_e = 4$eV.

We observe also that there other reasons for A_a^{eff} to become even smaller than A_a. For, from Eq. (57) we can deduce, assuming for the moment that the j_1 species dominates the ion currents,

$$j_e A_e \approx j_1 A_1 \tag{58}$$

$$\frac{A_e}{A_1} \approx \frac{v_1}{\frac{1}{4} v_e} \approx 1.4 \times \left(\frac{m_e}{m_1}\right)^{1/2} \approx \frac{1}{40} , \tag{59}$$

where v_1 is given by Eq. (12) and we use $m_1 = 2$ amu. In Eq. (58) we merely state the requirement that the flux of electrons leaving the system must be balanced by that of ions. Now the sources we have studied have the typical value $A_a/A_w \sim 1/10$. Hence

$$A_e \approx A_a^{eff} \sim \frac{1}{4} A_a , \tag{60}$$

where A_a is the geometric anode area. Part of this reduction of effective anode area may be due to the positive plasma potential mentioned above, but this can account for no more than a factor of 1/2. Other reasons for this discrepancy are unclear to us; a possible explanation may be the partial shielding of the anode by the magnetic field caused by the arc current or the filament current. In any case we determine A_a^{eff} self-consistently by demanding that n_e calculated from Eq. (41), plus the total primary n_p calculated from Eq. (32), Eq. (37), etc., to be equal to the sum of ion densities in Eq. (20). This A_a^{eff} is then used in Eq. (42) to determine the output kT_e.

D. Source Performance Parameters

It is useful to use the following quantities to characterize the performance of an ion source:

$$1.\ \text{Atomic Fraction} = \frac{j_1}{\sum_i j_i} \times 100\% , \tag{61}$$

$$2.\ \text{Gas Efficiency} = \frac{(j_1 + 2\,j_2 + 3\,j_3)A_I}{2F} \times 100\%\ , \tag{62}$$

where A_I is the ion current extraction area, and F is the flow rate, in the unit given by Eq. (25), and

$$3.\ \text{Arc Efficiency} = \frac{I_{arc}\ V_{arc}}{\sum_i j_i A_I}\ \ \text{eV/ion}\ . \tag{63}$$

The arc efficiency is the amount of energy needed to produce each ion extracted. Alternatively, if, instead of A_I, we use A_i, the total ion loss area, then we get a quantity which tells us the average amount of energy needed to produce each ion created in the source. Sometimes, as in the case of a magnetic bucket source, the ion wall loss area is not the geometric area, so we need more measurements or assumptions about the effectiveness of the ion confinement for this latter definition of arc efficiency to be useful.

One can also define the following:

$$\text{Ionization Efficiency} = \frac{I_{arc}}{I_i} = \eta, \tag{64}$$

$$\eta^{-1} \approx \frac{j_{p1}A_{p1} + n_{p1}[N_1 S_1' + N_2\,(S_2' + S_3') + N_2\,Q_2')]\ V}{n_e(N_1\,\tilde{S}_1 + N_2\,\tilde{S}_3)\ \ V} \tag{65}$$

$$\xrightarrow[N_2>>N_1]{} \frac{n_{p1}(S_2' + S_3' + Q_2')}{n_e \tilde{S}_3} + \frac{1}{N_2}\,\frac{j_{p1}A_{p1}}{n_e\,\tilde{S}_3} \equiv A + \frac{B}{p}\ , \tag{66}$$

where p is the gas pressure. The form on the right in Eq. (66) was also obtained by the Culham group.[14]

IV. APPLICATIONS

We now seek quantitative results for the model when it is applied to certain specific ion sources. Let us summarize the input information needed:

a) For all the sources we studied, we shall treat the following quantities as phenomenological constants:

1. The ion velocity factor s_w in Eq. (12).
2. Neutral temperatures kT_1 and kT_2.
3. Wall recombination coefficient γ.

b) For a given source, we need

1. The source geometry: V, A, A_{anode}, A_{wall} (including the areas of filaments and filament supports), A_I and A_0. (In the case of the magnetic bucket source more information is needed; this will be discussed below.) A_0 includes the gas transmission probability -- see Eq. (30).

2. The source "operation point": F, I_{arc} and V_{arc}.

The numerical procedure goes like this: we first guess a set of starting values for n_e, kT_e and n_{pl}, typically $n_e=2.0\times10^{12}$ cm^{-3}, kT_e = 4 eV, and n_{pl}/n_e = 0.1. They are used in Eq. (48) through Eq. (52) to calculate the five densities of ions and neutrals. Then we calculate the primary electron densities from Eq. (32), Eq. (37) and so on, n_e from Eq. (41), kT_e from Eq. (42), and, if needed, the floating wall potential from Eq. (43). Then these latest values are used as input to repeat the iteration until a self-consistent result is obtained with desired accuracy.

Now we present some results of the calculations:

A. TFTR-Project Source

This is a large conventional source[15] with a cross section 54.6 cm x 15.88 cm and a depth of 8.57 cm. The front and side walls are electrically connected to the negative ends of the filaments; part of the back plate, with an area of 474 cm^2, serves as anode. The beam-extraction area is 240 cm^2. In Fig. 4 we compare the result of the model calculation with data as a function of arc power for a given flow rate of D_2 gas. We also show the sensitivity of the computed current fractions of the species as the wall recombination coefficient γ assumes three different values. The total j is virtually independent of the choice of γ. Clearly the choice $\gamma = 0.2$ produces results in better overall agreement with data.[16] (We will use this value of γ from now on in our discussion, unless otherwise specified.) Also shown in Fig. 5 are the calculated kT_e, the ratio N_1/N_2 and the degree of dissociation y of the D_2 gas, defined as

$$y = \frac{N_1}{N_1 + 2N_2} \tag{67}$$

as a function of arc power. Unfortunately, for this source there are no measured data for these quantities for comparison. In Table 1 we show some input and output quantitities of the model for a typical operating point of this source.

B. LBL 10-amp Ion Source

This is a cylindrical source[17] with a radius of 7 cm and a total depth of 7.8 cm, of which a 1.8 cm long section of annular area near the front grid serves as anode. The extraction area is 29.4 cm^2. There are data about local kT_e and charge density from probe measurements

near the center of the plasma, but no systematic species measurement of an extracted ion beam has been made. In Figs. 6 and 7 we show the observed (local) and calculated (average) quantities as a function of arc power and flow rate respectively. In general the calculated kT_e's are a bit lower than those observed. This difference suggests there may be some other heating mechanism of secondary electrons that we have not taken into account. On the other hand, during that particular set of probe measurements, there was no neutralizer, so the neutral gas flowing back into the source was less than assumed in the model. If we use a larger A_0 than that given by Eq. (30), we would get a slightly higher kT_e.

C. Magnetic Bucket Source

We choose to consider here a "Big Bucket" Source B[18] with a cross section 52.7 cm x 23.0 cm and a depth 24.1 cm. The front plate is electrically floating, and the extraction area of 240 cm^2. The other five sides serve as the anode, and have rows of bar magnets on the exterior surfaces to provide some degree of confinement for the plasma inside. The magnets on the sides are arranged to form longitudinal cusp lines separated from each other by 4 cm, whereas the magnets on the back are aligned diagonally. The pole strength at the inner walls (alternating N and S) is about 2900 gauss.

The question as to how the magnetic cusp arrangement "confines" the various species of charged particles in the plasma is a complicated subject.[19] It lies outside the scope of particle balance equations and warrants a separate study. Here we shall content ourself with a few empirical observations, to be used as input for the source model calculation.

With the typical arangement and strength of magnets described above, it has been observed[20] that the plasma density, which has a quite constant value from the center to about 7 cm distant from the wall, drops to zero at the wall in a more or less linearly fashion between two cusp lines. No such drop is observed at the cusp lines themselves. The density full-width-half-maximum recorded by sweeping a Langmuir probe across one cusp line at the wall has been measured to be about 0.3 cm.[21] This "leakage width" is several times the ion gyroradius, e.g., $r_i \sim 0.1$ cm if $kT_i \sim$ leV. Also there may be different leakage widths for the energetic primary electrons, which are harder to observe.

For the model calculation, we take into account the effect of the magnetic field in the following manner. Picture an imaginary surface, recessed from the actual surface (except the front plate) by half the fall-off distance of the plasma density; there in the above-mentioned case this imaginary surface is 3.5 cm from the wall. Inside this reduced surface we treat the volume as field-free. We assume that this reduced surface is partially transparent to ions and electrons. Lacking better information, we simply adjust the loss areas to give agreement between the calculated and observed ion current densities at one arc power and flow rate. These loss areas are then held constant for other operating points. There is also another complication. From Eq. (15) and Eq. (31) we can deduce that the density of D_1^+ can be represented approximately as

$$n_1 \propto \frac{1}{A_1 A_{p1}} \quad . \tag{68}$$

Thus if the product of A_1, the loss area of D_1^+, and A_{p1}, the loss area of the (original) primaries, is kept constant, the model gives nearly identical results. One can have a model with weak confinement of ions and strong confinement of primary electrons, or more moderate confinement of both, and obtain satisfactory results in both cases. (Remember that the confinement of secondary electrons is determined by the charge neutrality condition, as explained in Sect.III.C). Indeed we have chosen several pairs of A_1, A_{p1} as inputs to the model and the calculated results are equally acceptable, as far as ion current densities are concerned. The pair that has a smaller A_{p1} gives rise to a higher primary density, but it is not easy to confirm this experimentally from probe measurement. We are inclined to choose the pair with a value of A_1 consistent with the one measurement of leakage width mentioned above; this choice has $A_1 \approx A_{p1} \approx 17\%$ of A, the geometric area. Furthermore, slightly better results are obtained by using $kT_1 = 0.60$ eV as observed for a bucket source. In Fig. 8 we compare some measured data with calculated results (shown as a function of arc power), and also show extrapolated performance at higher arc powers. In Fig. 9, the variation of measured and calculated quantities with gas flow is shown for the same source but without magnets on the back: "Big Bucket" Source A; (thus the whole back plate, minus some edge area, is a loss area for ions and electrons). We should add that we get results which agree equally well with data when we apply the same rule to two other magnetic bucket sources, a source exactly double in depth as the one studied here, and a square bucket with side length 24 cm.

D. Exploratory Calculations

Both the data and calculation show the following trends of source performance:

1. The total j first increases about linearly with arc power, then the rate of increase becomes smaller.

2. The fraction of D^+ ions arriving at the front wall seems to have a saturation value for each source. After a certain arc power, further increase of the j_1 fraction only comes from the decrease of the j_3 fraction, whereas the j_2 fraction (not j_2 itself) remains constant. For example, for the Big Bucket source, j_1/j_{total} = 80% is about the maximum we can achieve, no matter how high the arc power is. A similar trend has been observed by others.[22]

3. The j_1 fraction is rather insensitive to the gas flow for fixed arc power. When we increase the gas flow, we merely convert more D_2^+ into D_3^+ by reaction No. 6.

4. For a given total j, the j_1 fraction is an increasing function of the volume-to-surface ratio. (For the case of a bucket source, the reduced volume and surface are used.) In Fig. 10, we plot this trend for D_2 with j = 0.26 amp/cm^2. The data seem to lie on the calculated curve, which was obtained by scaling the three dimensions of the TFTR-Project source and recalculating the anticipated performance with the model.

5. Changing from a conventional source to a bucket source improves the gas efficiency and the arc efficiency. For example let us compare the characteristics of two sources for j=0.26 amp/cm^2:

	TFTR-Project Source	"Big Bucket" Source B
size	8.57cm x 54.6cm x 15.9cm	24.1cm x 52.7cm x 23.0cm
F	22 Tor-L/s	10 Torr-L/s
$I_{arc} x V_{arc} = P_{acr}$	2300amp x 56 volt=128.8 kW	1350ampx76 volt = 102.6 kW
D_1^+ fraction	65%	77%
Gas eff.	37%	66%
Arc eff.	2556 eV/ion	1730 eV/ion
Ion. eff.	0.37	0.39

After having gained some confidence in the model calculation, we now proceed, using the Bucket Source A as a reference, to do some exploratory calculations for other source designs with the aim of improving the source performance.

1. Double Bucket

From Fig. 10 we see that making the source larger in size will raise the j_1 fraction, but increasingly slowly. For example, changing from the "single bucket" to "double bucket" (making the source twice deeper) increases the j_1 fraction from 76% to 79% for $j=0.26$ amp/cm^2. This has since been confirmed by experiments.

2. Predissociation

If the D_2 gas fed into the source is predissociated to some extent, then one may hope that there will be an increase in the j_1 fraction because there should be an increase in the density of D_1 atoms available for ionization. This modification requires adding the following term to the left-hand-side of Eq. (18):

$$\beta \cdot 2F/V \tag{69}$$

where $0 \leq \beta \leq 1$ is the degree of predissociation. However calculations indicate, however, that even in the ideal situation of complete

predissociation (β=1), the j_1 fraction only increases from 76% to 77.4% for j=0.26 amp/cm^2. This is because the D_1 atoms are readily recombined into D_2 at the wall. At steady state, the degree of dissociation of D_2, as defined in Eq. (67) is increased by only 10%, (from 0.30 to 0.33) by completely predissociating the input gas.

3. Hot Walls

We can see from the example above that we have to maintain a higher degree of dissociation of D_2 gas in order to have higher j_1 fraction. One way of achieving that is to make the inside surfaces of the source hot. If a wall is hot enough, it will dissociate the incident molecules, as well as reduce recombination of the incident atoms. Langmuir[23] showed that for a tungsten surface above about 2200^{0}K, a fraction d = 0.49 of incident H_2 leaves the surface as H_1. On the practical side, T. Takagi et. al.[24] proposed to use quartz as chamber wall, and surround it with heating coil and thermal radiation shield. J. Kim and R. C. Davis,[25] lined the surface in the cathode region with tungsten in a duopigatron source along with some othe improvements, and observed the H_1^+ fraction to increase from ~50% to ~70%.

We have used the model to study the question of the variation of the species fractions with wall temperature. The details will be reported elsewhere. Here we merely show the limiting case. For a neutral gas density of 10^{14} cm^{-3}, detail-balance arguments leads to d=0.45 and γ=0.01 for wall temperature = 2600^{0}K. If we have five walls of the reference source hot and the front wall cold (d=0.00, γ=0.20), then the j_1 fraction would be 94% for j=0.26 amp/am^2.

To summarize, we think heating the walls is an interesting approach, but it is also a difficult mechanical problem.

4. Dual Cathodes

Another method of maintaining a higher degree of dissociation of D_2 gas is by altering the energy distribution of the electrons to favor a higher degree of dissociation in the source volume. Notice in Fig. 2A, for the reaction $H_2 + e \rightarrow 2H + e$, the $\sigma \cdot v$ value is maximum at around 16 eV. Hence, if electrons of this energy are injected into the plasma in addition to the usual primary electrons of the arc, then these electrons would dissociate more D_2, but would not make more D_2^+ because the energy is too low.[26] In order to maintain a given j output, the main arc current must be reduced if we add this subsidiary arc current. The calculated result is shown in Fig. 11 for $j = 0.26$ amp/cm^2. The j_1 fraction can be raised from 76% to 83% by this technique.

We think this is a viable approach, and some recent data on a low arc current source support this conclusion.[27]

5. Low Arc Impedance

By reducing the arc impedance (by changing the filament design or temperature, for example), it is possible to improve the arc power efficiency. We have done some calculations corresponding to such a change. For example, for $j = 0.26$ amp/cm^2, if we change:

from $V_{arc} = 52$ volt, $I_{arc} = 1700$ amp, $Z = 0.03$ ohm, $P = 88.4$ kW

to $V_{arc} = 30$ volt, $I_{arc} = 2200$ amp, $Z = 0.01$ ohm, $P = 65.4$ kW

then we get the same j but with j_1 fraction larger by 2 percentage points, (because the lower arc voltage favors more dissociations.) There is an improvement in arc efficiency.

But we also realize that V_{arc} cannot be too low, or the arc would not start. Furthermore, for lower V_{arc} a larger I_{arc} is needed for the same number of filaments, which has an adverse effect on filament life.

6. RF-generated Plasma

Plasma can also be generated by radio-frequency waves[28] instead of by electrons from the cathodes. Let us assume the ionization and dissociation processes in such a source in steady state are dominated by a thermal distribution of electrons. This corresponds in our model to having no primaries, but only secondary electrons. Instead of using the arc power as input, we now have to adjust kT_e to give the desired j, whereas n_e is fixed by the charge-neutrality condition. For a typical source such as the TFTR-Project Source mentioned above, the predicted performance is shown in Fig. 12. While the electron temperature is relatively high, it is amazing that, for the same j, the beam composition is practically the same as that of the conventional source, as shown in Fig. 4. Here we have used $\gamma = 0.2$ again. However, this need not be the case since there is no tungsten deposition on the walls. If the walls are made of pyrex glass[12] and $\gamma = 0.001$, then the j_1 fraction would be substaintially higher. For example, for j = 0.26 amp/cm^2, j_1 fraction changes from 65% to 83%. Thus by proper choice of wall materials, it may be possible to produce a high j_1 fraction from an RF-heated discharge, a condition difficult to achieve with a source using hot tungsten filaments.

E. Hydrogen Gas

Thus far we have focused our attention on the application of the model to D_2 gas because this isotope is most useful for MFE neutral beam injection, and we have data in abundance. We only have relatively few cases for H_2 gas operation in which we have complete measurements (ion current, species fractions, etc.)

One of the cases is the conventional TFTR-Project source. We chose to study this one because there is no additional complication due to the external cusp magnetic field confinement of ions. We have seen that the model can account quantitatively quite well for the D_2 data, as shown in Fig. 4. When we apply the model in a straight forward manner (just by changing the masses of the ions and neutrals), we find that the computed j's are lower than the observed ones by as much as one-third, and that the calculated species fractions disagree with the measured ones.

A closer examination of the problem reveals that one of our previous assumptions may be no longer true. We have assumped that the plasma potential is alway equal to, or slightly (1 or 2 volts) above the anode potential. However, we have reason to believe that for the H_2 case, for the same source under similar operating conditions, the plasma potential may actually fall somewhat below the anode potential, which tends to prevent the ions from reaching the anode. In that case we have less ion loss and hence more ion current arriving at the front and sides. Referring back to Eq. (57) and Eq. (58), we have

$$j_e A_a \exp\left[+(\phi_a - \phi_0)/kT_e\right] \approx \sum_i n_i v_i A_i \ , \qquad (70)$$

where ϕ_a is the anode potential, and ϕ_0 is the plasma potential. Now if we switch from D_2 to H_2 gas, and if the kT_e in two cases are

about the same, for like gas flow rates, then the v_i's increase by a factor of $2^{1/2}$. (We have seen above that the output is not sensitive to flow rate changes. In any case we don't expect kT_e to change by a factor of 2 as the masses do.) Thus, from Eq. (70) we have

$$\phi_o^D - \phi_o^H \approx kT_e \ln 2^{1/2} = 0.35\, kT_e \,. \tag{71}$$

Hence, the plasma potential in the H_2 case will be about 2 volts lower than that in the D_2 case for $kT_e \sim 5$ eV. Intuitively, because the hydrogen ions are lighter, and move out of the plasma volume faster; this must be balanced by more rapid loss of electrons, which are lost almost exclusively to the anode. This balance is achieved by a change in the plasma potential, which will become negative with respect to the anode, such that the anode will be more attractive to the electrons, and will repel the ions to reduce ion loss. Indeed we have data[29] on the 24 cm Square Bucket Source taken with H_2 and D_2 at similar flow rates to lend some credence to this argument:

	I_{arc}	V_{arc}	P_{arc}	n_e	kT_e	ϕ_o(w.r.t.ϕ_a= o)
D_2	370	56	20.7	1.2×10^{12}	3.8	+0.76
H_2	320	60	19.2	0.9×10^{12}	3.6	-0.50 .

If we delete the anode as a loss area for the ion species, i.e. set $A_a = 0$ in Eq. (27), then our model gives about the correct j. However, the agreement between calculated and observed species fractions is still not as good as the case for D_2 gas, as can be seen in Fig. 13.

For the calculated result, the j_3 fraction is too large, and the j_1 fraction too small. We don't know whether this is due to the greater nonuniformity of the plasma, or some isotope effect that we are not aware of. The neutral temperatures should be essentially the same. (see Appendix B). If we change the wall recombination coefficient γ to 0.05 for H_2, then we get agreement as good as in the D_2 cases. This γ value is actually very close to that for H_1 recombination on tungsten surfaces quoted above in Sect.II.B.4. The apparent big difference between the $\gamma = 0.20$ for D_1 and $\gamma = 0.05$ for H_1 needed in our model is a puzzle to us; we do not know if this is reasonable or not from the point of view of surface chemistry.[30]

V. CONCLUSIONS

For the plasma in question, there are many competing atomic and molecular reactions, with rapidly varying rate coefficients. We have constructed a model incorporating the relevant physics and have used the computer to handle the bookkeeping work of dealing with these input quantities and to solve the resulting system of equations. From the results presented above, we see that the model is able to generate the observed values of current densities, electron temperature and species fractions. In most cases the calculated values agree with the data within the estimated uncertainties in the measurements.

We have not attempted to calculate the neutral temperatures. We have treated them as constants, although they actually vary slowly with arc power. Fortunately the outcome of the model is not very sensitive to these changes, since they enter the equations only through the square root function in Eq. (21) and Eq. (22).

We have taken the values of I_{arc} and V_{arc} from experimental readings, and have not tried to calculate them self-consistently, as they can be varied over a wide range by change in gas flow, filament temperature, etc.

We have done several calculations exploring ways to improve the design of these sources. These calculations serve as indicative examples and of course are not an all-inclusive list. We would like also to remark that, by including other relevant reactions, the model could be modified to study the case of negative ion (D^-, H^-) sources.

We have seen that it is not easy to raise the D_1^+ fraction substantially. The basic reasons are that i) the walls in the plasma

chamber act as steady convertors of atoms into molecules, and ii) it is just as easy to ionize a D_2 as it is to ionize a D_1. From the model calculations it is clear that the D_1^+ ions come more likely from the dissociation of D_2, followed by the ionization of D_1, than from the ionization of D_2, followed by the dissociation of D_2^+. For example, for the TFTR-Project Source mentioned in Sect. IV A, we find for the reaction rate ratio (rather insensitive to arc power)

$$\frac{D_1 \rightarrow D_1^+}{D_2^+ \rightarrow D_1^+} \sim \frac{N_1}{n_2} \frac{n_p}{n_e} \frac{S_1'}{S_1} \sim 10^2 \times 10^{-1} \times \frac{3 \times 10^{-8}}{1 \times 10^{-7}} = 3.$$

For the Bucket Source mentioned in Sect.IV C, this ratio is about 1.5, mainly because the ratio N_1/n_2 is smaller.

From this study we have gained a deeper insight into the same basic properties of the plasma in question, the atomic physics involved, and into why ion sources perform as they do. For the purposes of seeking reality and utility, we believe this is an useful addition to the wealth of accumulated empirical facts[31] about atom and ion sources in general.

Acknowledgments

We thank members of the LBL-MFE group for fruitful discussions, especially K. N. Leung, A. F. Lietzke, D. Massoletti, P. A. Pincosy and M. C. Vella, and also J. R. Hiskes of LLNL. We are also grateful for the advice of Wulf B. Kunkel.

Appendix A: Some Remarks on the Reactions and Cross Sections

A detailed tabulation of the data of the cross sections and computed rate coefficients will be reported elsewhere.[32] Here we just make a few remarks.

1. We use the formula

$$S = 6.6923 \times 10^{7}(kT_e)^{-3/2} \int_0^{\infty} dE\ E\ \sigma\ \exp(-E/kT_e), \qquad (A1)$$

where S is in cm^3/sec, kT_e and E and in eV, and σ is in cm^2.

2. For reaction No. 7, the measurement[33] was made only for the production of protons. Therefore we should have at least two final channels

$$H_3^+ + e \rightarrow H^+ + H_2 + e$$
$$\rightarrow H^+ + 2H + e \quad .$$

We choose to neglect the second channel because it is energetically less favorable. This has little effect on the population of H_2 or H because their densities are usually one or two orders of magnitude larger than that of H_3^+.

And, for reaction No. 8, the measurement[34] was made for the neutral final states

$$H_3^+ + e \rightarrow H_2 + H$$
$$\rightarrow 3H \quad .$$

For the same reason stated above, we choose to ignore the second channel.

3. For the heavy particle reaction No. 6,

$H_2^+ + H_2 \rightarrow H_3^+ + H$,

there exist two groups of data. The first group came from the tandem mass spectrometer (TMS) experiment of Giese and Maier[35] of Chicago. The second group came from the merging beam (MB) experiment of Gentry, McClure and Douglas[36] of Minnesota, as well as earlier experiment by Neynaber and Trujillo.[37] The cross sections from the MB experiments are smaller than those from the TMS experiment by a factor of about 2.4. (The comparison is made with the connection $E_{Lab} = 2\ E_{cm}$ between the two groups of data). Gentry et al.[36] argued that "no inconsistency necessarily exists since the merged beam cross sections apply only to the peculiar distribution of H_2 internal states which arises from high-energy charge transfer neutralization of H_2^+." On the other hand, the thermal H_2 used in TMS experiment is more probably in the ground state, in which case it more closely resembles the situation of our ion sources. We therefore choose to use the cross sections from the Chicago group. As a test we also tried to use the cross sections from the Minnesota group in our model and found that these cross sections are unable to generate enough H_3^+ current density to match the source data.

We have two additional notes concerning this reaction:

a) We used an empirical expression[35] for the cross section:

$$\sigma = \sigma_0 \exp(-\alpha E), \qquad \text{(A1)}$$

with $\sigma_o = 8.2 \times 10^{-15}$ cm^2, $\alpha = 0.42$, $E = E_{Lab}$ of the ion.

b) There is no apparent isotope effect[38], therefore

$$\sigma^{D_2}(E) = \sigma^{H_2}(E). \tag{A2}$$

Now as for the rate coefficient of this reaction, let us consider the case of a drifting Maxwellian gas (H_2^+) with temperature kT_1 and drift velocity v_d interacting with a stationary Maxwellian gas (H_2) with temperature kT_2. Then

$$S = \int d^3\vec{v}_1 d^3\vec{v}_2 \, |\vec{v}_1 - \vec{v}_2| \;\; \sigma(|\vec{v}_1 - \vec{v}_2|) \; f_1 f_2$$

$$= \pi^{-3/2} \, v_\mu^3 \int d^3\vec{v} \; v\sigma(v) \; \exp[-(\vec{v}-\vec{v}_d)^2/v_u^2]$$

$$= \pi^{-1/2} \, v_\mu^{-1} \, v_d^{-1} \int_o^\infty dv \; v^2 \; \sigma(v) \left\{\exp[-(v-v_d)^2/v_\mu^2] - \exp[-(v+v_d)^2 v_\mu^2]\right\}, \tag{A3}$$

where

$v_\mu = (2kT_1/m_1 + 2\,kT_2/m_2)^{1/2}$,

$\vec{v}$ = The relative velocity vector, $v = |\vec{v}|$, and

$\vec{v}_d$ = the drift velocity vector, $v_d = |\vec{v}_d|$.

Equation (A3) is useful in the general situation.

If now we rewrite Eq. (A1) as $\sigma = \sigma_o \exp(-v^2/v_o^2)$, with

$v_o^2 = 2 \times 1.19/\mu$, and recall $v_d^2 = 2\,E_d/m_1$, $E_d \gtrsim 1$ eV,

whereas $kT_{1,2} \sim 0.1$ eV, we have

$$S \approx v_d \sigma_o \exp(-v_d^2/v_o^2)\ \mathrm{erf}\ (v_d/v_\mu) \tag{A4}$$

$$\approx v_d \sigma_o \exp(-0.42\ E_d) = v_d\ \sigma(E_d), \tag{A5}$$

because $\mathrm{erf}(x) \sim 1 - \pi^{-1/2}\ x^{-1}\ e^{-x^2} + \ldots.$

We used this value for S in the model, with the value for v_d as given by Eq. (12).

Appendix B

Measurement of the Neutral Atomic and Molecular Deuterium Temperatures

The temperature of the atomic deuterium in a 14 cm diameter by 7.8 cm deep multifilament conventional ion source (the LBL 10-amp Ion Source) was measured by monitoring the Doppler broadening of the D_β 4860Å line with a Fabry-Perot interferometer. The piezoelectrically driven Fabry-Perot was housed in a temperature-controlled oven and had a finesse of 30. The line emission was observed on an axial optic axis looking through the accelerator slots of the ion source.

The profile of the D_β line was close to a Gaussian in shape. The temperature was determined by comparing the experimental line profile with a calculated profile which was a convolution of the Gaussian Doppler broadening with the fine structure[39] of the D_β line and the Stark broadening profile.[40] The atomic deuterium temperature was found to increase weakly with the arc power (Fig. 14) and had a value of $kT_1 = .35 \pm .06$ eV at an arc power of 31 kW for a gas flow of 6 Torr-L/sec. We also looked for a shift in the line center of the emission from the discharge by comparison with a Fabry-Perot scan of a spectral lamp. There was a blue shift $.03 \pm .02$ Å for the 4680 D_β line. Presumably this is caused by a flow of gas toward the accelerator slots and corresponds to an average velocity of 1.85×10^5 cm/sec.

Several electronic collision processes can produce excited (n=4) deuterium atoms in the discharge:

1) $e + D_1 \rightarrow D_1^*$, excitation of ground state D atoms[41],

2) $e + D_2 \rightarrow D_1^*$, dissociate excitation of molecular deuterium[42],

3) $e + D_2^+ \rightarrow D_1^*$, dissociative recombination into an excited state.[43]

If the first process dominates, then the Doppler broadening of the D_β line is a true measure of the velocity distribution of deuterium atoms in the ground state. We have calculated the excitation rate per unit volume of the n=4 level for the source operated at 31 kW arc power and flow rate = 6.5 Torr-L/s (with I_{arc} = 800 amp, V_{arc} = 39 volts). We have estimated the parameters of the discharge from the results of the model calculation: $n_e = 3.4 \times 10^{12}$ cm^{-3}, kT_e = 4 eV, $N_1 = N_2 = 1.6 \times 10^{14}$ cm^{-3}, $n_2 = 6 \times 10^{11}$ cm^{-3} and f = 0.1 where N_1, N_2, n_2 is the density of D_1, D_2, D_2^+ respectively, and f is the ratio of the density of primary electrons to the bulk electron density. The contributions to the volume rate of excitation of the n=4 level are

$$R_1 = n_e N_1 [\langle\sigma_1 v\rangle + f \sigma_1 v_p] = 1.03 \times 10^{17} \text{ cm}^{-3}$$
$$R_2 = n_e N_2 [\langle\sigma_2 v\rangle + f \sigma_2 v_p] = 4.1 \times 10^{15} \text{ cm}^{-3}$$
$$R_3 = n_e n_2 \langle\sigma_3 v\rangle = 2.7 \times 10^{15} \text{cm}^{-3}$$

We find that processes (2) and (3) contribute 4% and 2.6% relative to the dominant process of excitation of ground state deuterium atoms under typical conditions in our experiment. In our experiment we also did not see evidence for a large population of cold (room temperature) atoms as reported by McNeill and Kim[44] for certain discharges.

Molecular deuterium lines were too weak to permit scanning of a molecular line during a single discharge. To measure the Doppler broadening of a molecular line we integrated the output of the photomultiplier tube, held the Fabry-Perot spacing constant during a single-discharge, and scanned the Fabry-Perot shot-to-shot. We chose to measure the broadening of the 5749.96 Å molecular deuterium line because it is relatively strong and isolated; also the nearby Ne 5748.65 A line provided a convenient calibration point to monitor drift of the Fabry-Perot. The molecular deuterium temperature increased from kT_2 = 0.09 eV to kT_2 = .12 eV as the arc power was increased from 15 to 56 kW (Fig. 15) for a gas flow of 6.5 Torr-L/s.

The Doppler broadening of the D_β line was also measured using an optical multichannel analyzer (PAR model 1215) coupled with a one-meter monochromator (Spex model 1704). With a 1200 groove/mm grating used in the third order, the system had a resolution of .038 A/channel. The Doppler broadening of the D_β line was determined by comparing the observed halfwidth of the line with the numerical convolution of the estimated Doppler width with the instrument, fine structure, and Stark broadening profiles.

To compare with the Fabry-Perot data, the Doppler broadening in the ion source was also measured with the monochromator and optical multi-channel analyzer. The line emission was viewed through a small slot in the side of the ion source; thus the optic axis was along a diameter of the cylindrical sidewall and transverse to the axis of the beamline. The results in Fig. 15 are very close to the earlier results at low power but somewhat hotter (~ 0.1 eV) at higher power levels. Cooling by wall collisions may produce an anisotropic velocity

distribution with higher temperatures transverse to the shorter axial dimension of the source.

The line emission from a magnetic bucket ion source, of dimensions 24 x 24 x 24 cm, was observed on an axial axis looking through the accelerator slots. The atomic deuterium temperature was measured both as a function of arc power at a gas flow of 3.5 Torr-L/sec and as a function of gas flow at a constant arc power of 28 kw. We also ran the discharge on hydrogen and measured the atomic hydrogen temperature as a function of arc power at a gas flow of 5 Torr-L/sec.

From the results shown in Fig. 16 we see an increase of the atomic temperature with arc power but the temperature is insensitive to charges in the gas flow (over the range studied) within experimental uncertainty. Comparing the hydrogen and deuterium data, we did not find a strong isotope effect with respect to neutral atomic temperatures in the magnetic bucket ion source. The most significant result is that the temperatures are approximately 50% higher in the magnetic bucket ion source than they are in the conventional ion source. This is probably not due to the magnetic confinement but rather to the larger dimension of the magnetic bucket ion source. Fast neutral atoms produced by dissociation of molecular deuterium are slowed by collisions with the walls. A detailed analysis of the processes which cause the velocity distribution of atoms in these discharges is complex, however we would expect the atomic temperature to increase as the volume to surface ratio of the source increases. In going from the conventional ion source to the magnetic bucket ion source the volume to surface ratio has increased from 1.6 cm to 4 cm, which may explain the higher atomic temperature in the later.

Appendix C: Various Contributions to the Secondary Electron Balance Equation

1. Mean Ejected Electron Energies from Ionization of Neutrals

J. D. Garcia[45] derived expressions for the ejected electron energy distributions from classical binary-encounter approximation. The results are very close to those obtained from the more complicated method of quantum mechanical Born approximations, and compare favorably with experimental data. From his expressions of $d\sigma/dE_2'$, where E_2' is the final kinetic energy of the ejected electron, we can compute $\bar{E}_2' = \int E_2' d\sigma / \int d\sigma$. If we use Garcia's Eq. (8), then we obtain

$$\bar{E}_2' = (\bar{\varepsilon} - 1)\, u \,, \tag{C1}$$

$$\bar{\varepsilon} = (\beta_1 - 1)\, \frac{3\, \mathrm{Ln}(\beta_1 - 1) - 3\, \beta_1 X + 10}{5(\beta_1 - 1) - 3} \,, \tag{C2}$$

where

u = the initial binding energy of the ejected electron,

E_1 = the initial energy of the ionizing electron, with the restriction $E_1 \geq 2u$ for Eq. (C2),

$\beta_1 = E_1/u$, and

$$X = \frac{1}{\beta_1^{1/2}}\, \mathrm{Ln}\, \frac{\beta_1^{1/2} + 1}{\beta_1^{1/2} - 1} \,.$$

Here are some typical values:

	E_1/u	= 2	3	4	5
	$\bar{E}'_2/u$	= 0.26	0.50	0.67	0.82
H_1(u=13.6 eV):	E_1	= 31.2	46.8	62.4	78.0
	$\bar{E}'_2$	= 4.1	7.8	10.5	12.8
H_2(u=15.6 eV):	E_1	= 27.2	40.8	54.4	68.0
	$\bar{E}'_2$	= 3.5	6.8	9.1	11.2

This question was also studied by C. B. Opal et al,[46] who found that the differential cross section for the ejected electron density distribution could be empirically represented as

$$\frac{d\sigma}{dE'_2} \propto \frac{1}{(E'_2 + E_o^2)} \quad ,$$

where E_o = 7.25 eV for H_2 target. This expression changes very slowly with E_1. Therefore from their work

$$\bar{E}'_2 = \frac{1}{2} E_o \frac{\text{Ln}\,[(E_1 - u)^2 / E_o^2 + 1]}{\tan^{-1}\,[(E_1 - u)/E_o]} \quad ,$$

which yields the following typical values:

H_2(u=15.6 eV):	E_1	= 31.2	46.8	62.4	78.0
	$\bar{E}'_2$	= 5.5	8.0	9.6	10.8 .

These results are quite close to those obtained from Garcia's expression.

Strictly speaking, we should put in primary-energy-dependent expressions for E_{s1} and E_{s2} in Eq. (42). This can be done, but for

the sake of simplicity we use the approximate average values $E_{s1} \approx E_{s2} \approx 7$ eV; this is the basis for Eq. (39). We found that the results are not sensitive to this choice.

2. Energy Transfer from Primary to Secondary electrons by Coulomb Collisions

The rate of energy loss of one primary streaming through a background of secondary electrons with density n_e is[47]

$$\frac{d}{dt} E_p = - \nu . E_p \ , \tag{C5}$$

where

$$\nu(x) = 7.7 \cdot 10^{-6} \ \Phi(x) \ E_p^{-3/2} \ n_e \ Ln\Lambda \quad ,$$

$$x = E_p / kT_e \ ,$$

$$Ln\Lambda = 23 - Ln(n_e^{1/2} \ (kT_e)^{-3/2}) \quad ,$$

$$\Phi(x) = \frac{2}{\pi}^{1/2} \left[\int_o^\infty dt \ e^{1/2} \ e^{-t} - \ 1/2 \ e^{-x} \right] \ . \tag{C6}$$

For large x, we have

$$\Phi(x) \gtrsim 1 - \frac{2}{\pi} x^{1/2} \ e^{-x} (2 + \frac{1}{2} x^{-1} - \ldots).$$

The power density transfered by a density of primaries n_p is then

$$P = E_p^{-1/2} \ n_p \ \Phi(x) \ n \ c \qquad eV.cm^{-3} \ . \ sec^{-1} \ , \tag{C7}$$

where

$$c = 7.7 \quad 10^{-6} \ Ln\Lambda \ .$$

3. Secondary Electron Energy Flux to the Wall

Suppose the wall has a potential -V relative to the plasma. Then the electron energy flux is

$$\int_{v_{min}}^{\infty} d^3v \, \frac{1}{2} mv^2 \, v_x \, f = \frac{1}{4} n \exp\left(\frac{eV}{kT}\right) \cdot \bar{v} \cdot (2kT + eV) \, , \tag{C8}$$

where

$$v_{min} = \left(\frac{2eV}{kT}\right)^{1/2} \, , \tag{C9}$$

$$f = \frac{n}{\pi^{3/2} v_{th}^3} \exp\left(-\frac{v^2}{v_{th}^2}\right) , \text{ and} \tag{C10}$$

$$v_{th} = \left(\frac{2kT}{m}\right)^{1/2} = \frac{\pi^{1/2}}{2} \bar{v} \, . \tag{C11}$$

4. Mean Electron Energy Loss Due to Recombinations

For reactions No. 4 and No. 8 listed in Section II.B.1, the cross section can be represented[48] in the form

$$\sigma(E) = \sigma_o E^{-\beta} \, . \tag{C12}$$

In this case the mean electron energy is

$$\bar{E} = \frac{\int_o^{\infty} dE \, E^2 \, \sigma \exp(-E/kT_e)}{\int_o^{\infty} dE \, E \, \sigma \exp(-E/kT_e)} = \frac{\int_o^{\infty} dE \, E^{2-\beta} \exp(-E/kT_e)}{\int_o^{\infty} dE \, E^{1-\beta} \exp(-E/kT_e)}$$

$$= \frac{(kT_e)^{2-\beta} \, \Gamma(2-\beta)}{(kT_e)^{3-\beta} \, \Gamma(3-\beta)} = (2-\beta) kT_e \, , \tag{C13}$$

where Γ is the gamma function and we have made use of the relation $\Gamma(x+1) = x\Gamma(x)$.

The numerical results are

Reaction	$\sigma_o(cm^2)$	β	$\bar{E}$
4. $H_2^+ + e \rightarrow 2H$	6.4×10^{-16}	1.4	$0.86\ kT_e$
8. $H_3^+ + e \rightarrow H_2 + H$	10.2×10^{-16}	0.87	$1.13\ kT_e$.

Footnotes and References

1. See the review by W. B. Kunkel, "Neutral-Beam Injection," in Fusion, Vol. 1, Part B, E. Teller, ed., Academic Press (1981).
2. A. R. Martin and T. S. Green, Culham Laboratory report CLM-R 159 (1976).
3. V. M. Kulygin and A. A. Panasenkov, Kurchatov Institute of Atomic Energy report IAE-2322/7 (1980).
4. S. Tanaka and T. Shibata, Japan Atomic Energy Research Institute Report JAERI-M 7966 (1978).
5. Various versions of this work have been reported by us: Bull. Am. Phys. Soc. 21, 1031 (1976); 23, 805 (1978); 24, 1016 (1979); 25, 982 (1980); 26, 989 (1981).
6. K. Smith and R. M. Thomson, Computer modeling of Gas Lasers, Plenum Publishing Corporation (1978); L. R. Peterson, Phys. Rev. 187, 105 (1969); L. R. Peterson and A. E. S. Green, J. Phys. B (Proc. Phys. Soc.), 1, 1131 (1968); A. Dalgarno and G. Lejeune, Plant Space Sci. 19, 1653 (1971).
7. L. Tonks and I. Langmuir, Phys. Rev. 34, 876 (1929).
8. S. A. Self, Phys. Fluids, 6, 1762 (1963).
9. C. F. Barnett, J. A. Ray, E. Ricci, M. I. Wilker, E. W. McDaniel, E. W. Thomas, and H. B. Gilbody, Oak Ridge National Laboratory reports ORNL-5206, 5207 (1977).
10. Kurt F. Schoenberg, Lawrence Berkeley Laboratory report LBL-7952 (1978), and Reference 17.
11. E. K. Shaw, Ph.D. Thesis, Stanford University (1967).
12. B. J. Wood and H. Wise, J. Chem. Phys. 29, 1416 (1958); ibid 65, 1976 (1961).
13. K. W. Ehlers and K. N. Leung, Rev. Sci. Instrum. 50, 356 (1979).

14. A. P. H. Goede, T. S. Green, and B. Singh, J. App. Phys 51, 1896 (1980).

15. MFE Neutral Beam Development Group, A Compilation of Operating Data for the TFTR-Project Source, LBL report LBID-154 (1979).

16. In order to correct for the openning area, we actually use $\gamma = \gamma + (1-\gamma) A_0/A$, where A is the total surface area.

17. K. F. Schoenberg and W. B. Kunkel, J. App. Phys. 50, 4685 (1979).

18. L. A. Biagi, K. H. Berkner, K. W. Ehlers, J. A. Paterson, and J. R. Porter, Proc. Eight Symposium on Engineering Problems of Fusion Research, 1979 (San Francisco, CA); IEEE Pub. No. 79CH1441-5-NPS.

19. See, for example, K. N. Leung, N. Hershkowitz and K. R. Mackenzie, Phys. Fluids, 19, 1045 (1976). Our plasma density is one to two orders of magnitude higher than that studied in this reference.

20. See, for example, K. W. Ehlers and K. N. Leung, Rev. Sci. Instrum, 50, 1353 (1979).

21. P. A. Pincosy, private communication.

22. D. Stork and R. S. Hemsworth, in the same proceedings as Ref. 18.

23. I. Langmuir, Phys. Rev. 40, 78 (1932).

24. T. Takagi, I. Yamada, M. Kunori, and S. Kobiyama, Proceedings of the Second Symposium on Ion Sources and Formation of Ion Beams, Berkeley, CA. (1974).

25. J. Kim and R. C. Davis, APPL. Phys. Lett. 30, 130 (1977).

26. This idea was suggested to us by K. N. Leung.

27. K. W. Ehlers and K. N. Leung, Rev. Sci. Instrum. 52, 1452 (1981).

28. See, for example, A. D. McDonald, Microwave Breakdown in Gases, John Wiley and Sons, Inc., (1966). We thank Ian Brown for explaining some of the physics to us.

29. We thank P. A. Pincosy for providing us with these data.

30. One may wonder how a factor of 2 in the mass ratio between D_1 and H_1 could produce such a big difference in the surface recombination coefficients, if it is true. However, a recent paper by R. DiFoggio and R. Gomer, Phys. Rev. B 25, 3490 (1982), (see also Scientific American, August 1982), concerning the diffusion of hydrogen and deuterium atoms on the (110) plane of tungsten may be related to the question here. These authors observed that under certain condition the surface diffusion coefficient of D_1 can be larger than that of H_1 by as much as three orders of magnitude. We conjecture that because the D_1 can diffuse faster along the surface, it has more chance to encounter another adsorbed D_1 with which it recombines to form D_2 and evaporates back to the plasma volume.

31. For example, L. Valyi, Atom and Ion Sources, Wiley-Interscience (1977).

32. C. F. Chan, LBL report LBID-632 (in preparation).

33. B. Peart and K. T. Dolder, J. Phys. B 7, 1567 (1974); ibid 8, L143 (1975).

34. B. Peart and K. T. Dolder, J. Phys. B, 7 1948 (1974).

35. G. F. Giese and W. B. Maier, J. Chem. phys. 39, 739 (1963).

36. W. R. Gentry, D. J. McClure and C. H. Douglass, Rev. Sci. Instrum., 46, 367 (1974).

37. R. H. Neynaber and S. M. Trujillo, Phys. Rev. 167, 63 (1968).

38. R. P. Clow and J. H. Futrell, Int., J. Mass Spectrom. Ion Phys. 8, 119 (1972).

39. H. A. Bethe and E. E. Salpeter, Quantum Mechanics of One and Two-Electron Atoms, p. 274, Springer-Verlay, Berlin, (1957).

40. W. L. Wiese, "Line Broadening" in Plasma Diagnostic Techniques, Eds. R. H. Huddlestone and S. L. Leonard, Academic Press, N.Y., 1965.

41. L. C. Johnson, Astrophys. J. 174, 227 (1972).

42. C. Karolis and E. Harting, J. Phys. B 11, 357 (1978).

43. R. A. Phoneuf, D. H. Crandall, and G. H. Dunn, Phys. Rev. A 11, 528 (1975).

44. D. H. McNeill and J. Kim, Phys. Rev. A 25, 2152 (1981).

45. J. D. Garcia, Phys. Rev. 177, 223 (1969).

46. E. B. Opal, E. C. Beatly and W. K. Peterson, Atomic Data, 4, 209 (1972).

47. David L. Book, NRL Plasma Formulary, Revised (1978).

48. B. Peart and K. T. Dolder, J. Phys. B, 7, 236 (1974); See also Ref. 34.

TABLE CAPTIONS

Table 1. Some input and output quantities of the source model for a typical operating point of the TFTR-Project Source. The units are the same as those used in the text. The mean free path, for example, for the dissociation of D_2 due to secondary electrons is computed from the expression $v_{02}/n_e S_2$. The total mean free path for the destruction of D_2 due to volume reactions is $\Lambda_2^{-1} = \sum_k \Lambda_{2k}^{-1}$, where the sum is for reactions No. 2, 3 and 6. (In this table we only list those reactions which contribute directly to Eq. (15-18).

INPUT:

$\gamma = 0.20$ $kT_1 = 0.35$ $kT_2 = 0.12$ $kT_i = 1.00$

$F = 22.0\ (D_2)$ $P_{arc} = 102.4$ $I_{arc} = 1970.0$ $V_{arc} = 52.0$ $\phi_w = -52.0$

OUTPUT:

$N_1 = 5.56 \times 10^{13}$ $N_2 = 6.23 \times 10^{13}$ $n_1 = 9.01 \times 10^{11}$ $n_2 = 5.10 \times 10^{11}$ $n_3 = 3.86 \times 10^{11}$

$n_e = 1.62 \times 10^{12}$ $n_p = 1.63 \times 10^{11}$

$kT_e = 4.67$

$j_1 = 0.132$	60.6%	Experiment:	63.2%
$j_2 = 0.053$	24.3%		24.1%
$j_3 = 0.033$	15.1%		12.7%
$j_t = 0.217$			0.218

	Reactions/cm^3-sec		Mean Free Path (cm)		
	Primaries	Secondaries	Primaries	Secondaries	Total
1. $D_1 + e \rightarrow D_1^+ + 2e$	1.95×10^{17}	5.92×10^{16}	187.0	616.0	$\Lambda_1 = 143.0$
2. $D_2 + e \rightarrow D_1 + D_1 + e$	9.71×10^{16}	3.78×10^{17}	174.0	44.7	
3. $D_2 + e \rightarrow D_2^+ + 2e$	2.82×10^{17}	6.98×10^{16}	60.0	242.0	$\Lambda_2 = 17.9$
4. $D_2^+ + e \rightarrow D_1 + D_1$	0.	9.42×10^{15}		35.1	
5. $D_2^+ + e \rightarrow D_1^+ + D_1 + e$	9.97×10^{15}	7.28×10^{16}	33.2	4.5	$\lambda_2 = 1.6$
6. $D_2^+ + D_2 \rightarrow D_3^+ + D_1$	1.17×10^{17}		$2.8(D_2^+)$	$145.0(D_2)$	
7. $D_3^+ + e \rightarrow D_1^+ + D_2 + e$	1.35×10^{16}	4.98×10^{15}	15.2	41.1	
8. $D_3^+ + e \rightarrow D_2 + D_1$	0.	1.05×10^{16}		19.5	$\lambda_3 = 7.1$

FIGURE CAPTIONS

Fig. 1 Schematic sketch of an LBL neutral beam ion source.

Fig. 2A Ionization and dissociation rate coefficients as a function of the (primary) electron energy. For the heavy particle reaction, E stands not for the electron energy but for the laboratory energy of H_2^+. The value of σ for this reaction is taken from Ref. 35. See Appendix A for more information.

Fig. 2B Electronic or vibrational excitation rate coefficients due to electron impact, as a function of the (primary) electron energy.

Fig. 3A Ionization and dissociation rate coefficients averaged over a Maxwellian electron distribution of temperature kT_e.

Fig. 3B Electronic or vibrational excitation rate coefficients due to electron impact, averaged over a Maxwellian electron distribution of temperature kT_e.

Fig. 4 Comparison between calculation (curves) and measured data of the current density and species current fractions as a function of arc power with three different assumed values for the wall recombination coefficient γ for the TFTR-Project Source. The gas flow rate was 22 Torr-L/s of D_2.

Fig. 5 The calculated kT_e and degree of dissociation of the D_2 gas, as a function of arc power for the TFTR-Project Source, at a flow of rate 22 Torr-L/s of D_2 gas.

Fig. 6 Calculated kT_e and n_e (curves) and measured data from probe measurements, as a function of arc power, for the LBL 10-Amp Source at F = 6.5 Torr-L/s D_2 gas.

Fig. 7 Calculated kT_e and n_e (curves) and measured date from probe measurements, as a function of D_2 gas flow rate, for the LBL 10-Amp Source at P_{arc}=22.6 kW.

Fig. 8 Comparison between calculation (curves) and measured data of the current density and species current fractions as a function of arc power for the "Big Bucket" Source at flow rate 10 Torr-L/s of D_2 gas.

Fig. 9 Comparison between calculation (curves) and measured data of the species current fractions as a function of D_2 gas flow rate, at P_{arc} = 51 kW for the "Big Bucket" Source without magnets on the back plate.

Fig. 10. D_1^+ current fractions as a function of the volume/surface ratios of the sources.

Fig. 11 "Dual Cathodes" scheme. The data points marked "original" stand for quantities with V_{arc} = 52 volt only.

Fig. 12 Calculated curent density and species current fractions as a function of kT_e for a RF-generated plasma source the size of the TFTR-Project Source.

Fig. 13 Comparison between calculation (curves) and data of current density and species current fraction as a function of arc power for the TFTR-Project Source at flow rate 30 Torr-L/s of H_2 gas. See also Footnote 30.

Fig. 14 Atomic and molecular deuterium temperatures versus arc power at a gas flow of 6 Torr-L/sec in the LBL 10-amp Ion Source (14 cm diameter x 7.8 cm deep). A. Molecular deuterium temperature. B. Atomic deuterium temperature.

Fig. 15 Atomic deuterium temperatures in the LBL 10-amp Ion Source (14 cm diameter x 7.8 cm deep) as viewed along an optic axis transerve to the beamline for A. as a function of gas flow at constant arc power of 22 kW, and B. as a function of arc power at constant gas flow of 6.5 Torr-L/sec.

Fig. 16 Atomic hydrogen and deuterium temperatures in a magnetic bucket ion source (24 cm cube), A. as a function of gas flow at constant arc power of 28 kW, and B. as a function of arc power at a gas flow of 3.5 Torr-L/sec for deuterium and 5 Torr-L/sec for hydrogen.

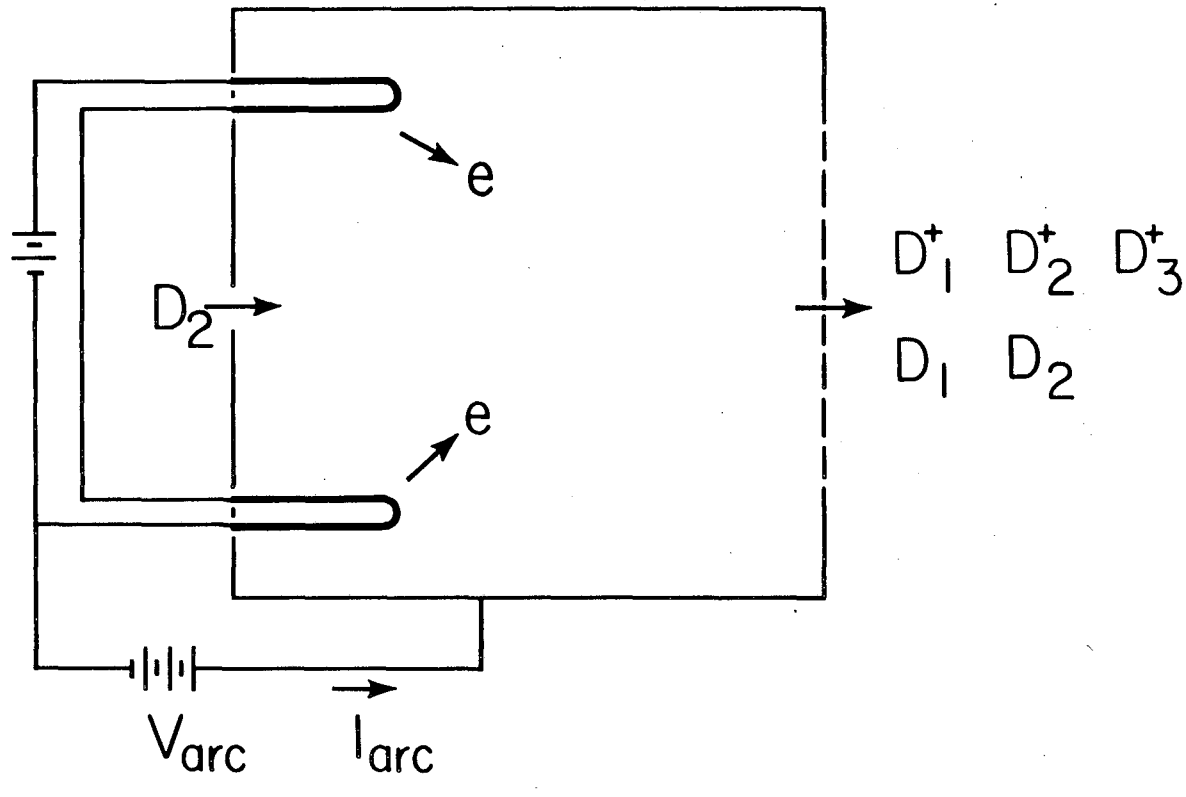

XBL 8210-2980

Figure 1

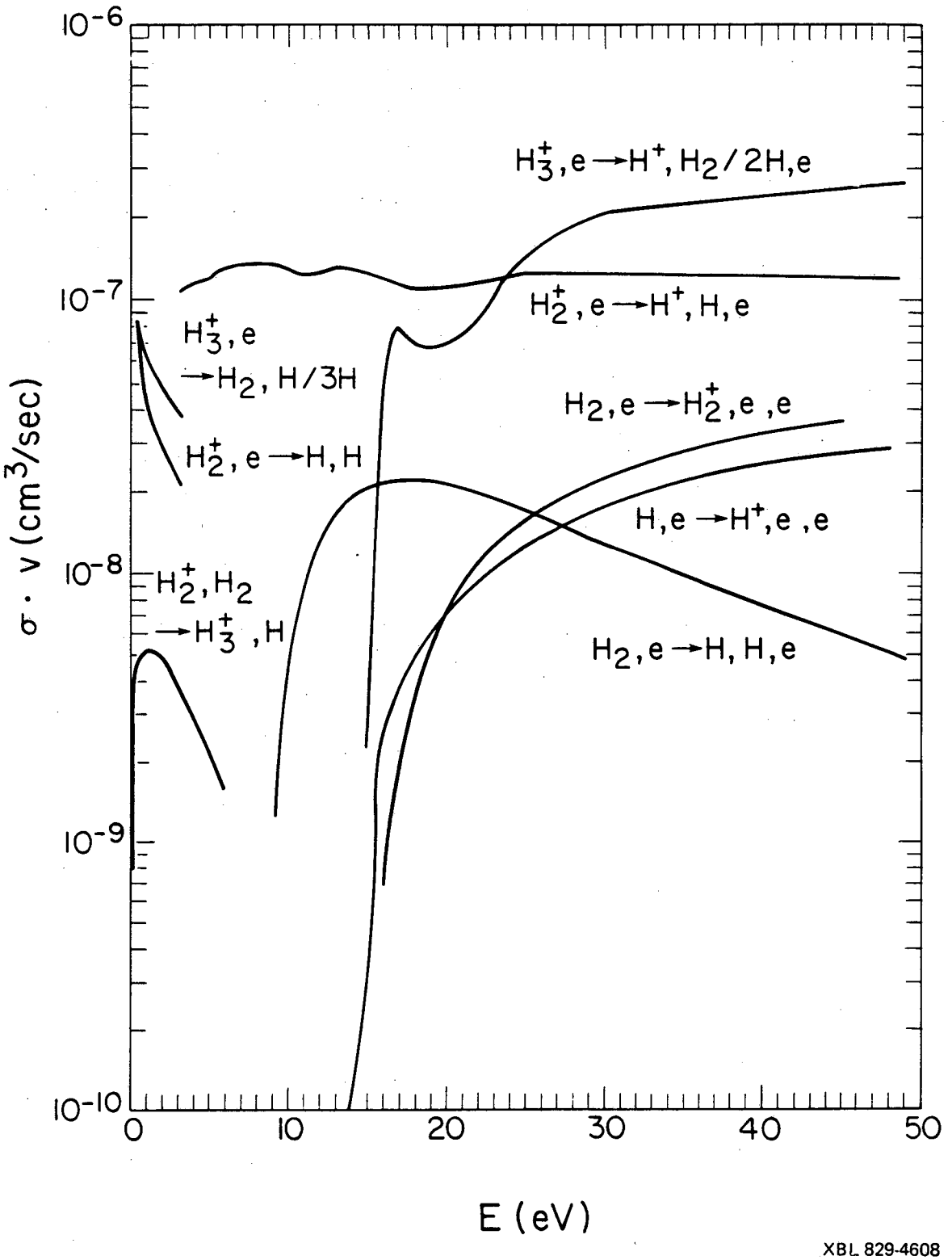
10^{-6}
10^{-7}
10^{-8}
10^{-9}
10^{-10}
$\sigma \cdot v$ (cm^3/sec)
$H_3^+, e \rightarrow H^+, H_2/2H, e$
$H_2^+, e \rightarrow H^+, H, e$
$H_3^+, e \rightarrow H_2, H/3H$
$H_2^+, e \rightarrow H, H$
$H_2, e \rightarrow H_2^+, e, e$
$H, e \rightarrow H^+, e, e$
$H_2^+, H_2 \rightarrow H_3^+, H$
$H_2, e \rightarrow H, H, e$
0
10
20
30
40
50
E (eV)
XBL 829-4608

Figure 2A

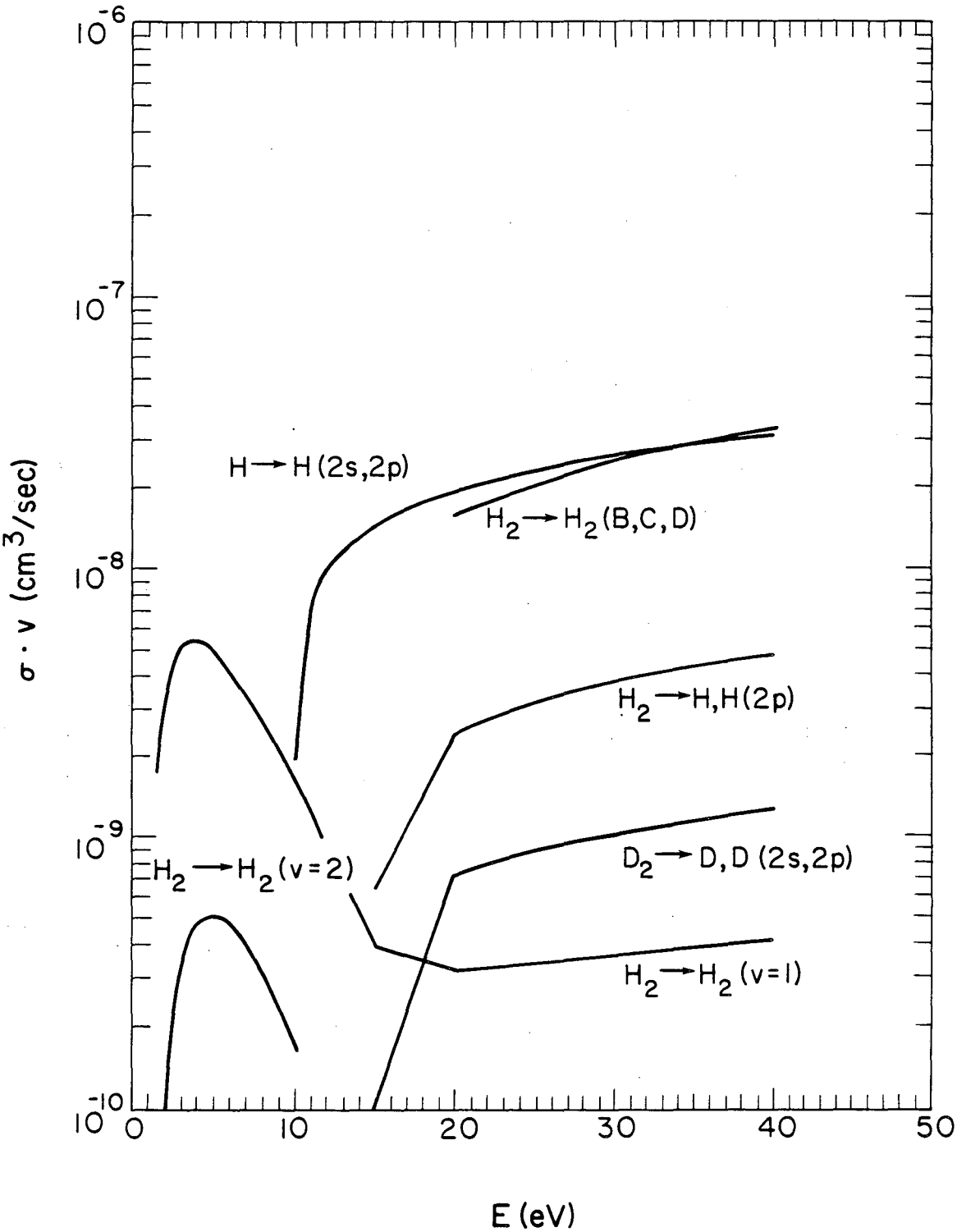

XBL 829-4605

Figure 2B

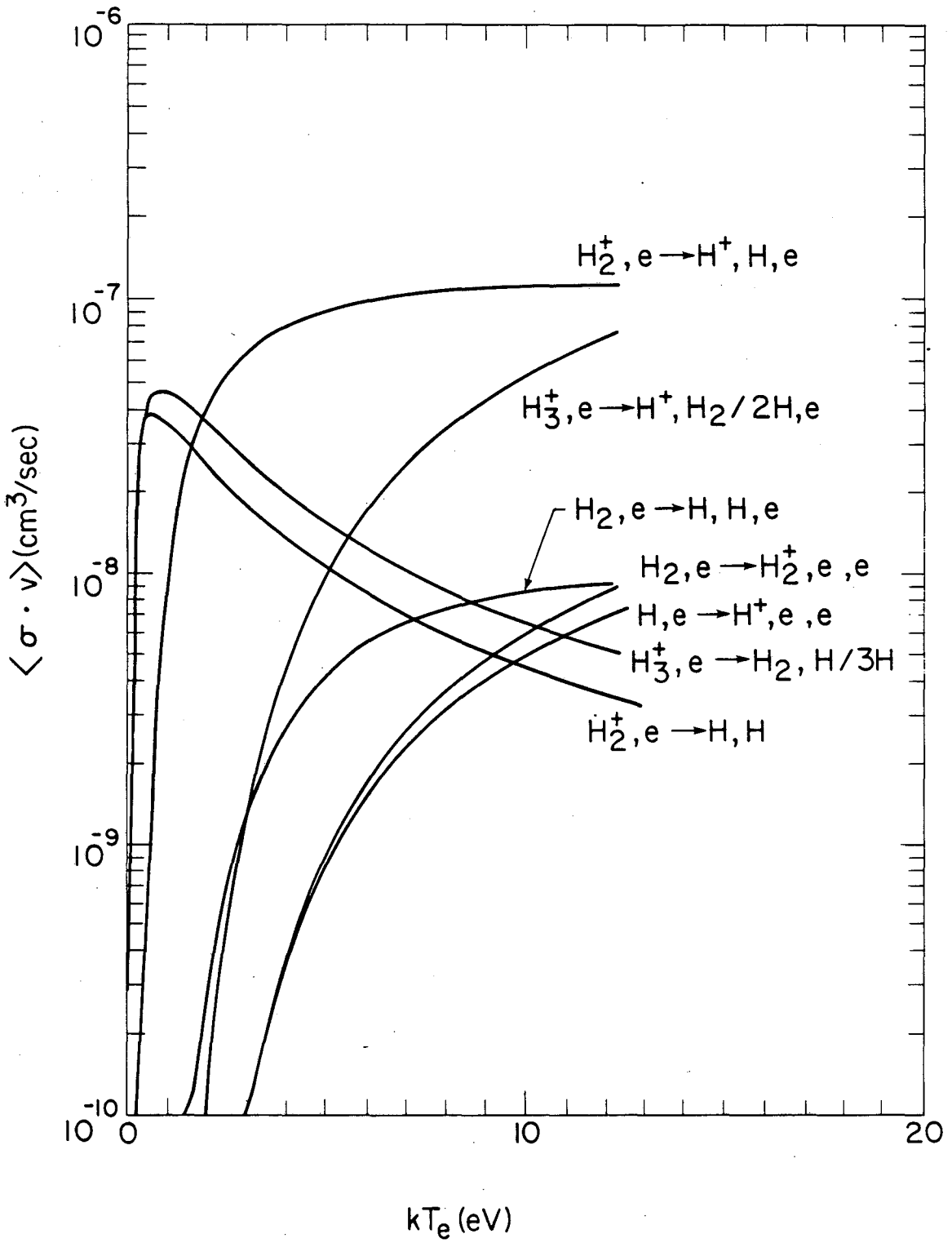

XBL-829-4587

Figure 3A

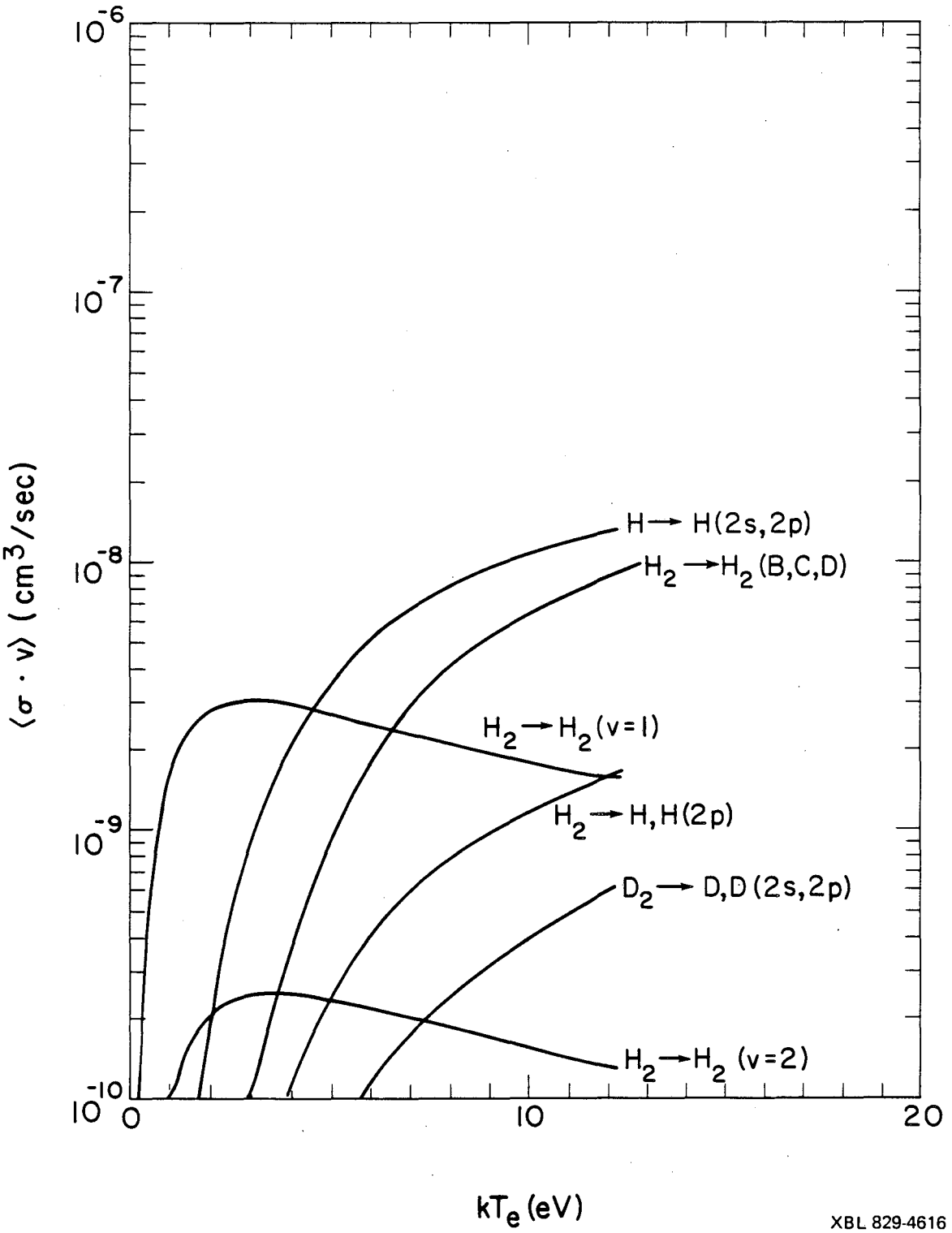
10^{-6}
10^{-7}
10^{-8}
10^{-9}
10^{-10}
$\langle \sigma \cdot v \rangle$ (cm^3/sec)
0
10
20
kT_e (eV)
H → H(2s,2p)
H_2 → H_2(B,C,D)
H_2 → H_2(v=1)
H_2 → H,H(2p)
D_2 → D,D(2s,2p)
H_2 → H_2 (v=2)
XBL 829-4616

Figure 3B

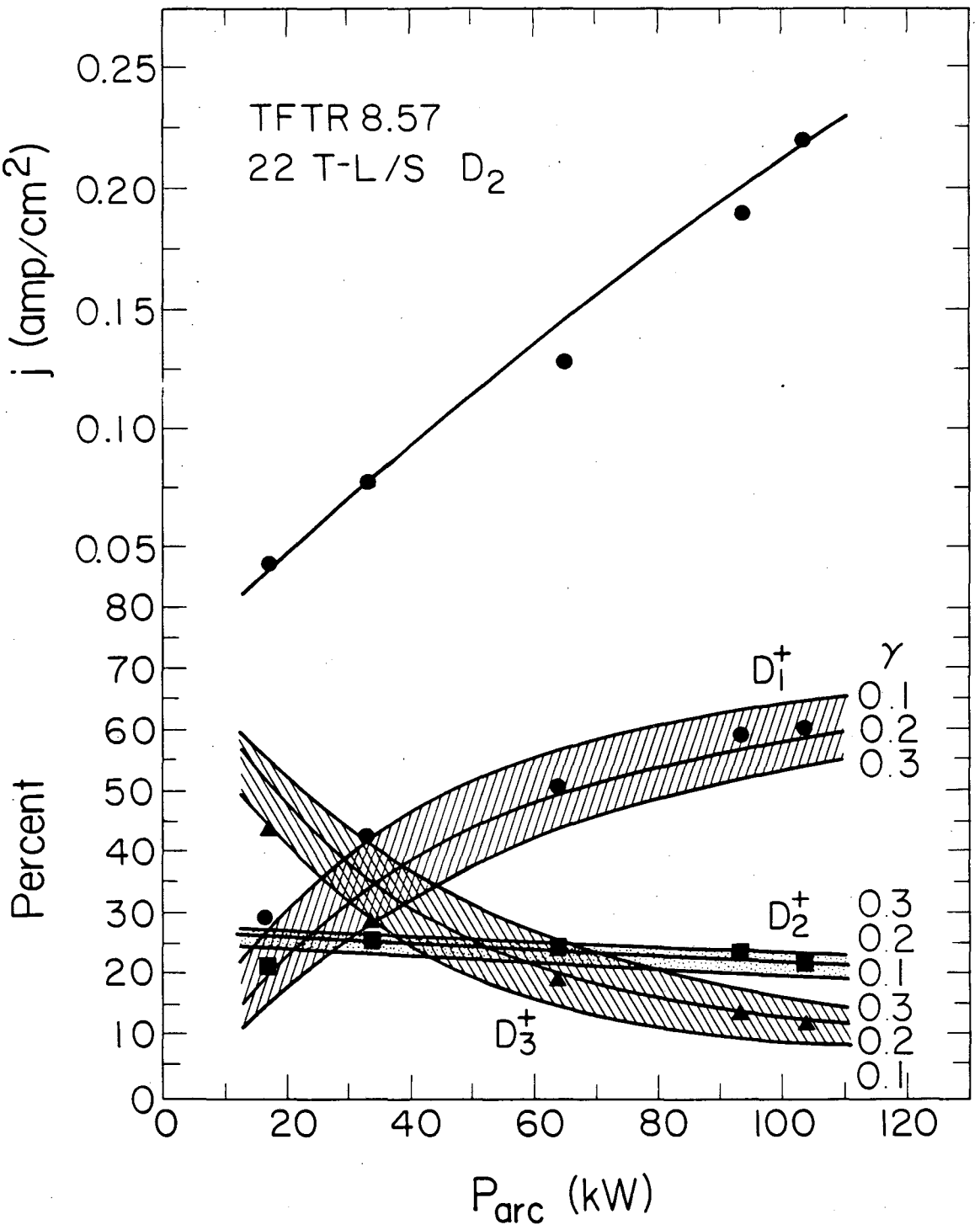

XBL 829-4606

Figure 4

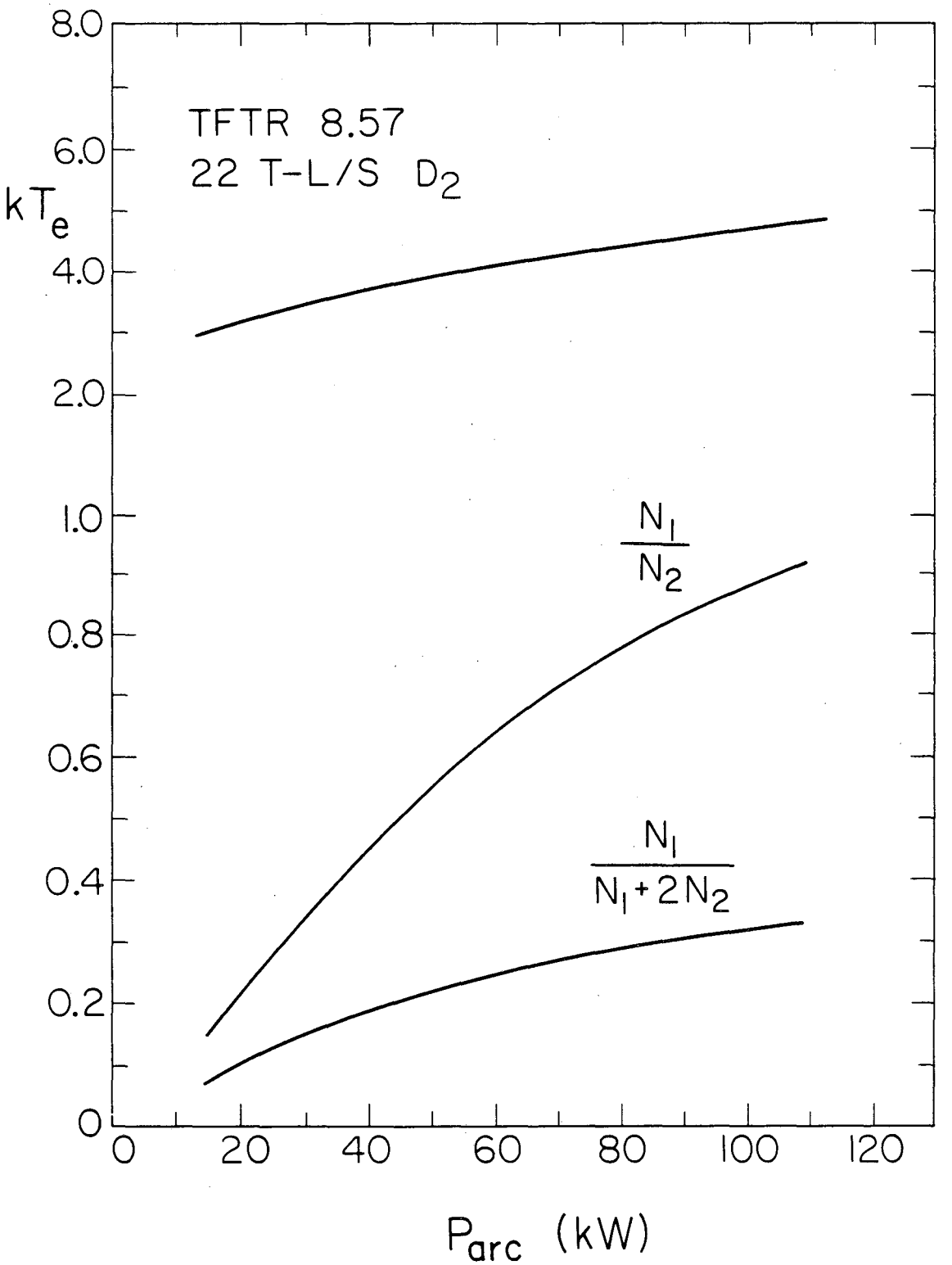

XBL 829-4581

Figure 5

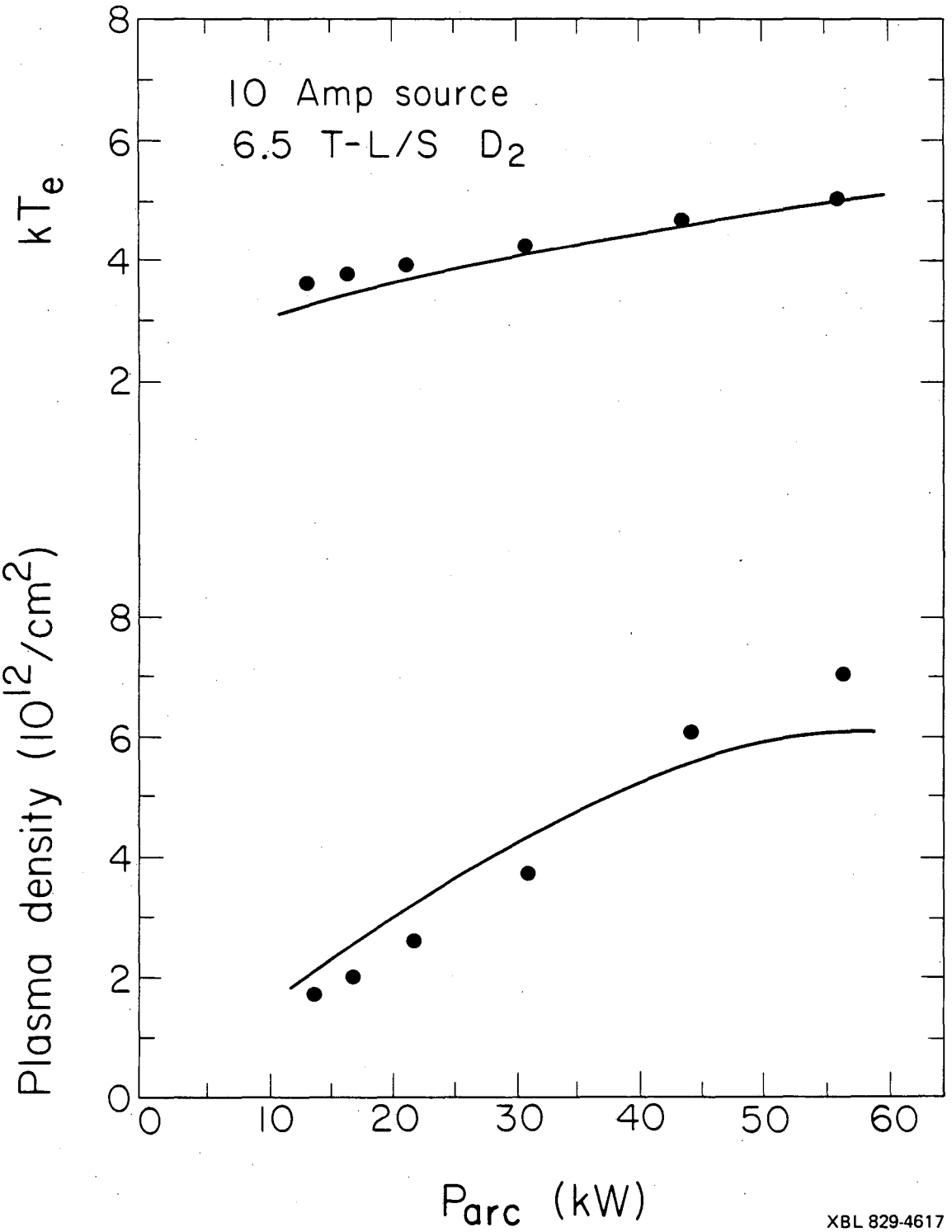
10 Amp source
6.5 T-L/S D_2
kT_e
Plasma density (10^{12}/cm^2)
P_{arc} (kW)
0
2
4
6
8
0
10
20
30
40
50
60
XBL 829-4617

Figure 6

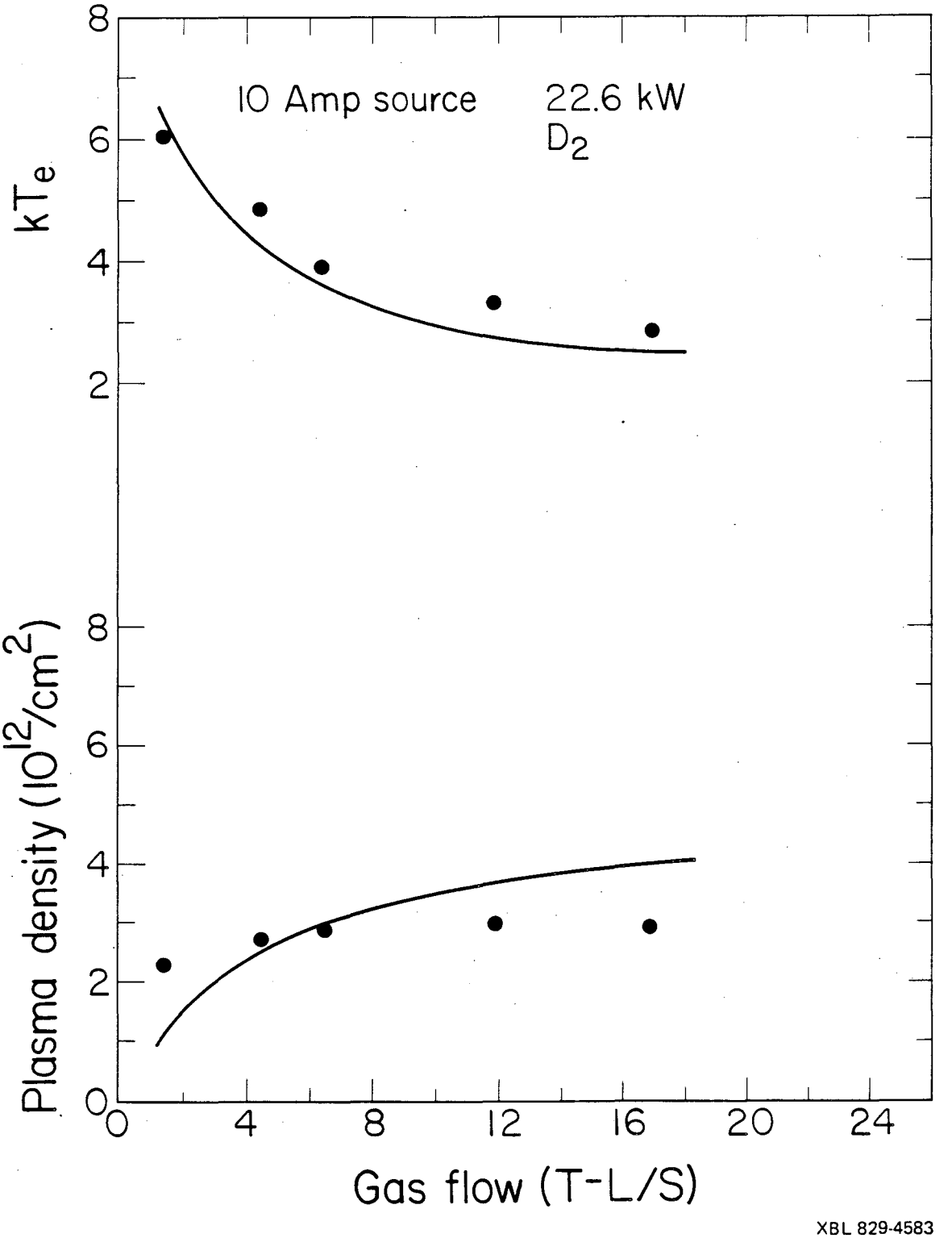
10 Amp source
22.6 kW
D_2
kT_e
Plasma density (10^{12}/cm^2)
Gas flow (T-L/S)
0
2
4
6
8
0
4
8
12
16
20
24
XBL 829-4583

Figure 7

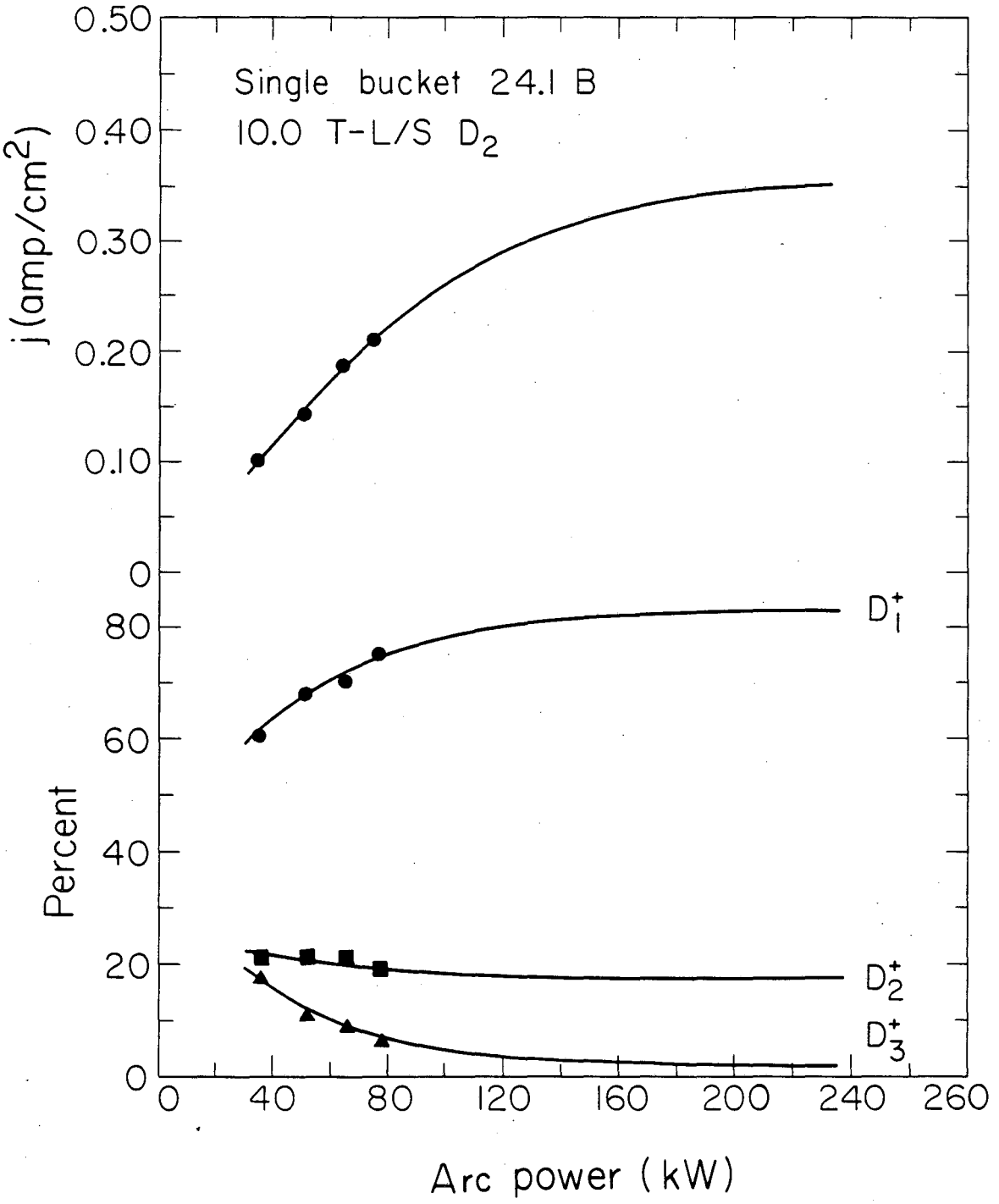

XBL 829-4579

Figure 8

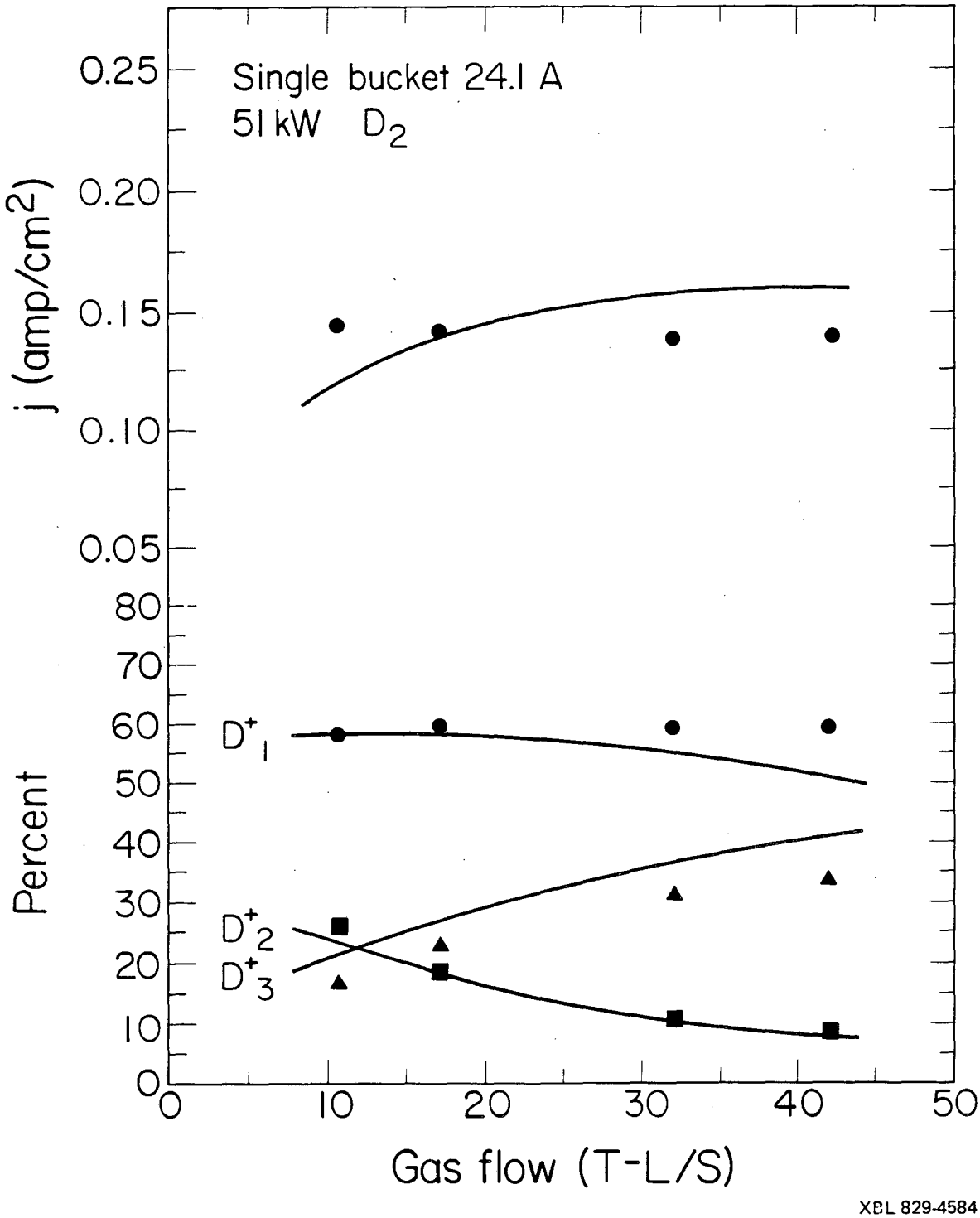

XBL 829-4584

Figure 9

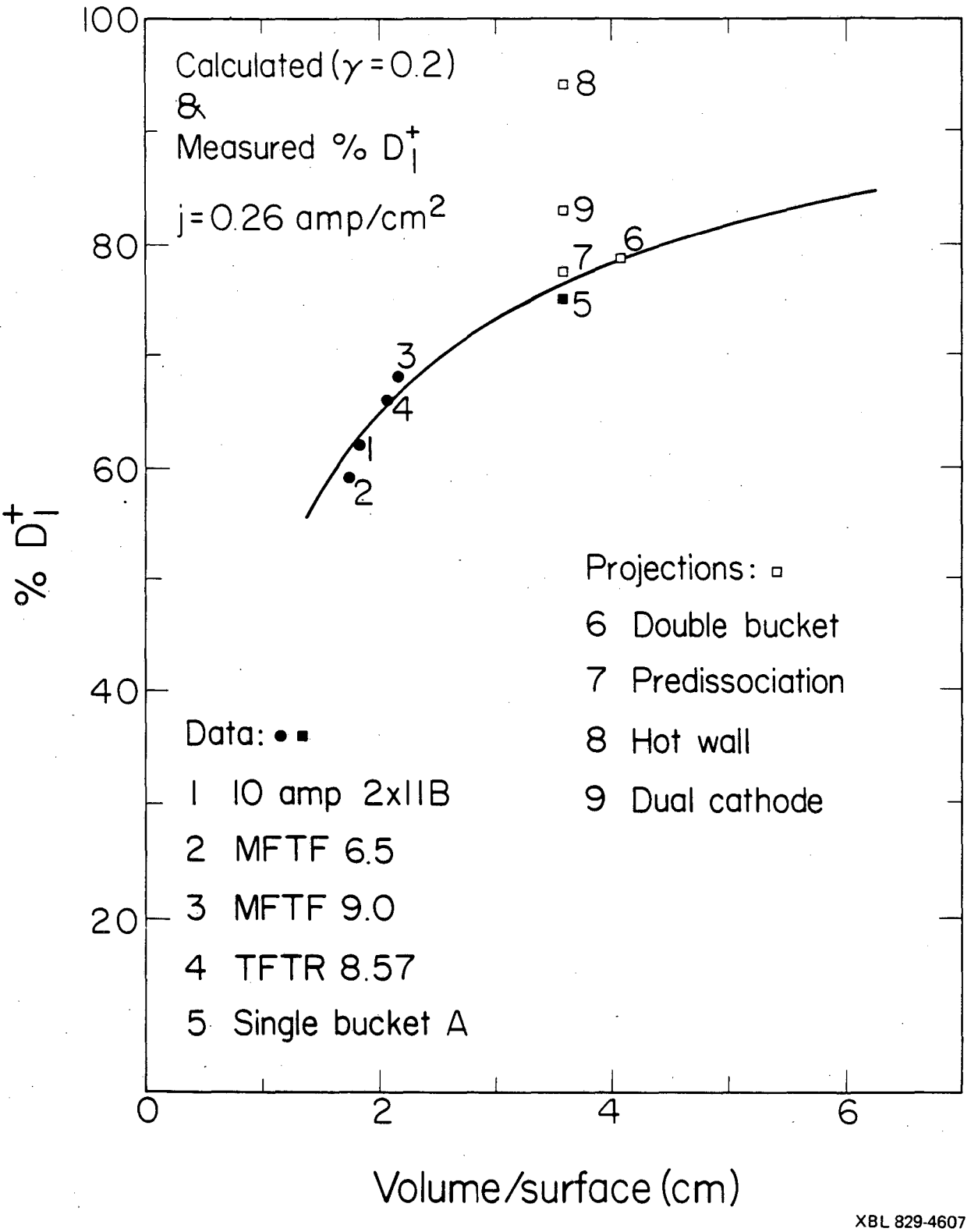
Calculated (γ = 0.2)
&
Measured % D_1^+
j = 0.26 amp/cm^2
Projections: □
6 Double bucket
7 Predissociation
8 Hot wall
9 Dual cathode
Data: ● ■
1 10 amp 2x11B
2 MFTF 6.5
3 MFTF 9.0
4 TFTR 8.57
5 Single bucket A
% D_1^+
Volume/surface (cm)
100
80
60
40
20
0
2
4
6
XBL 829-4607

Figure 10

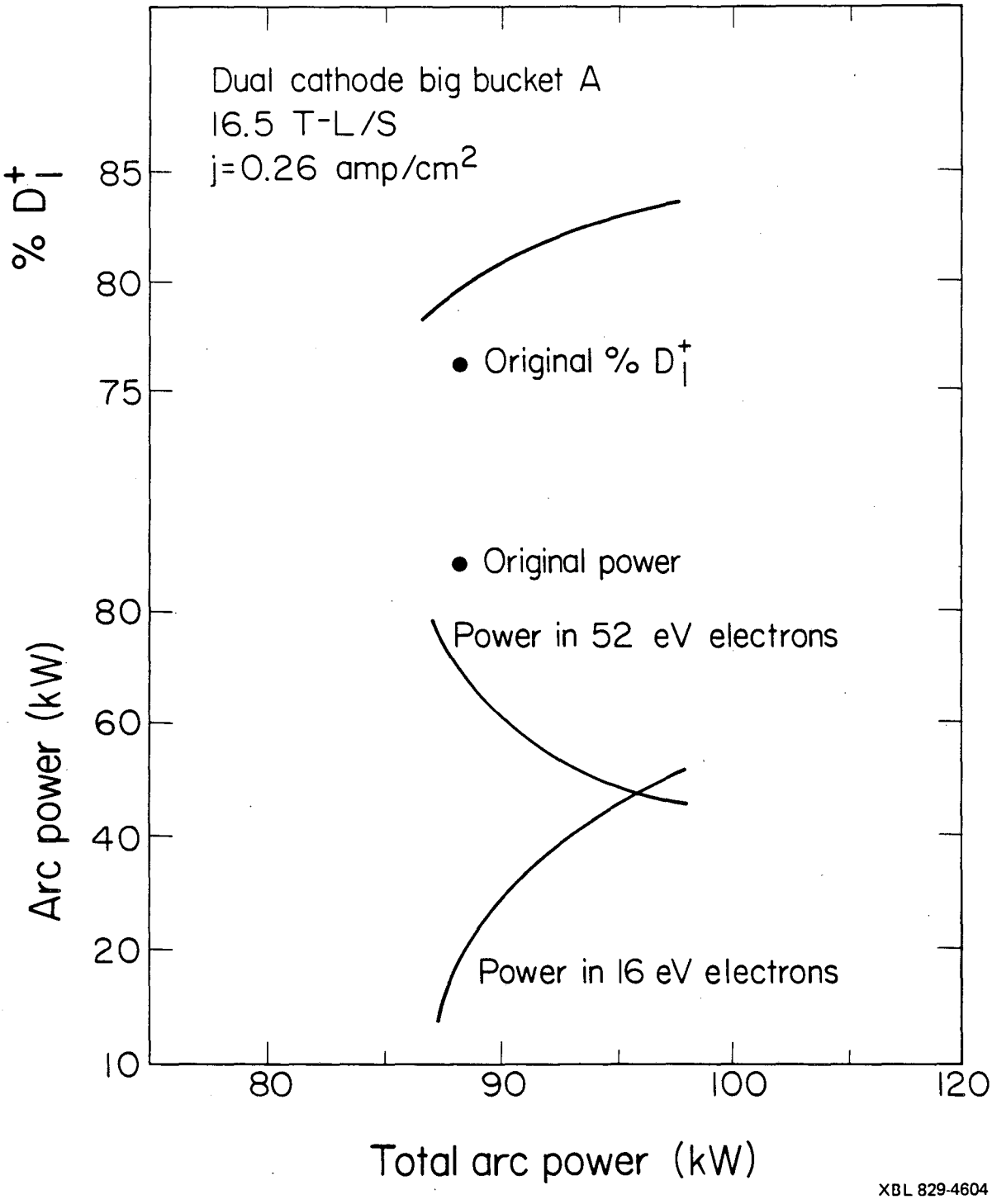
Dual cathode big bucket A
16.5 T-L/S
j=0.26 amp/cm2
% D1+
85
80
75
Original % D1+
Original power
80
60
40
20
10
Arc power (kW)
Power in 52 eV electrons
Power in 16 eV electrons
80
90
100
120
Total arc power (kW)
XBL 829-4604

Figure 11

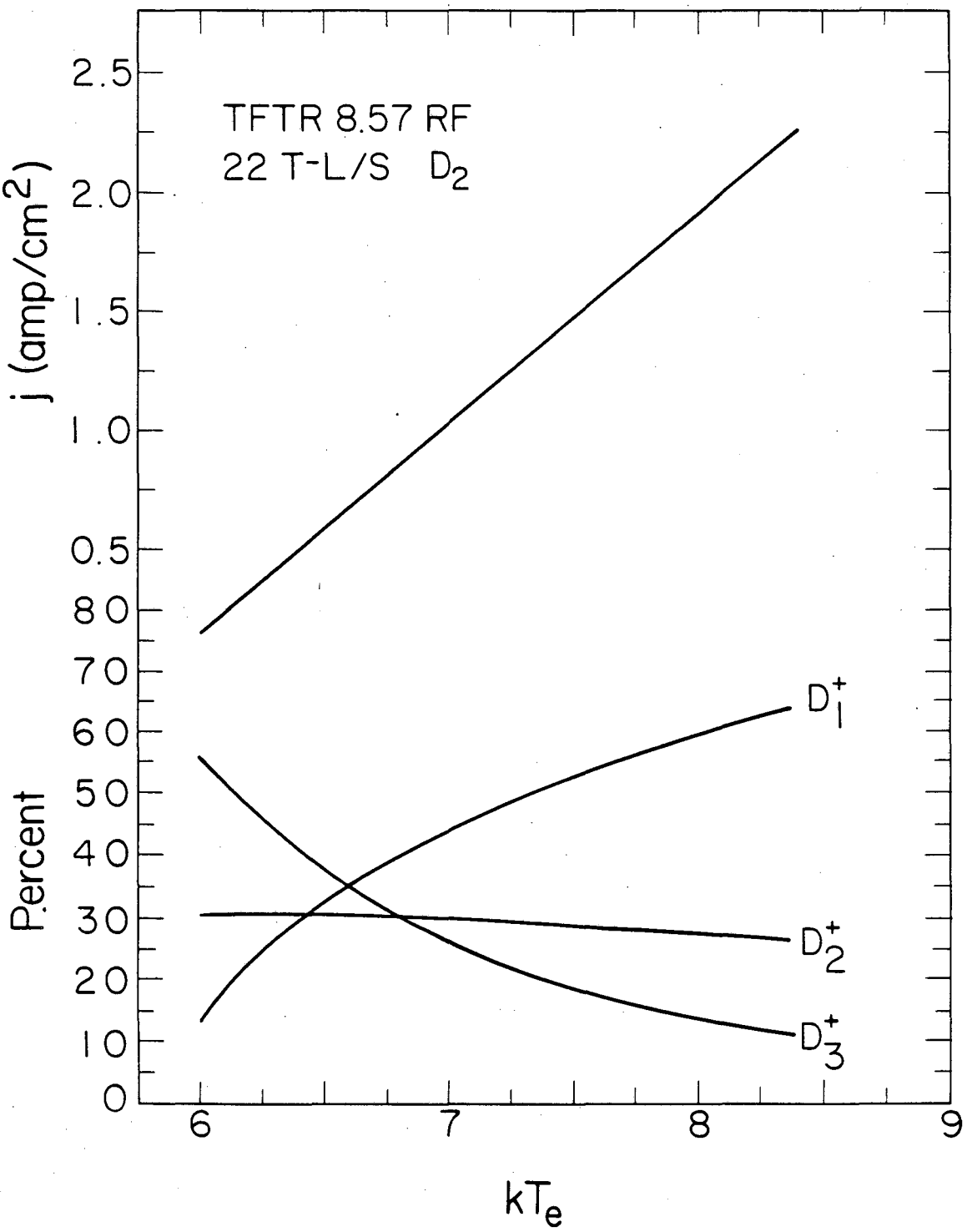

XBL 829-4602

Figure 12

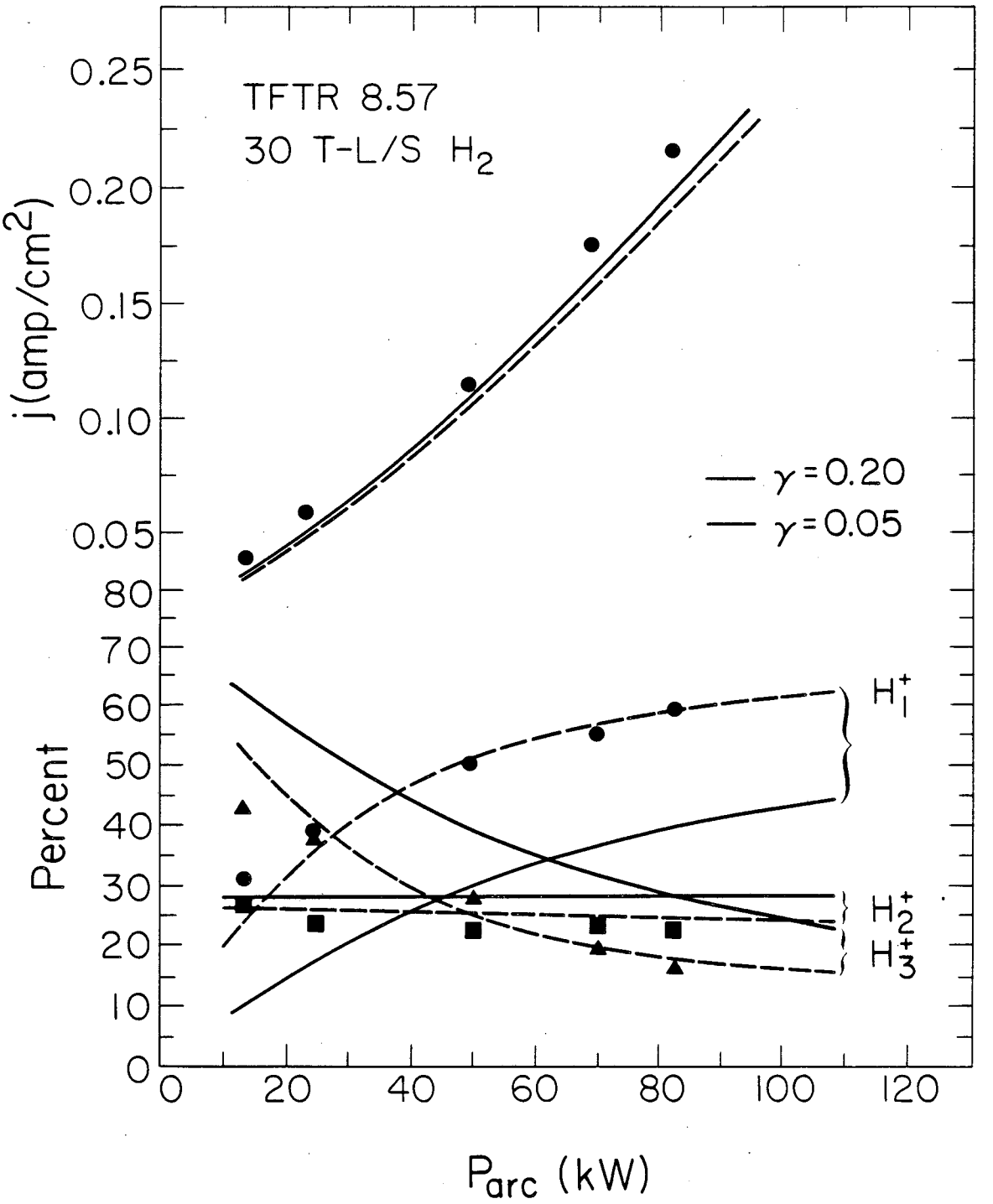

XBL 829-4580

Figure 13

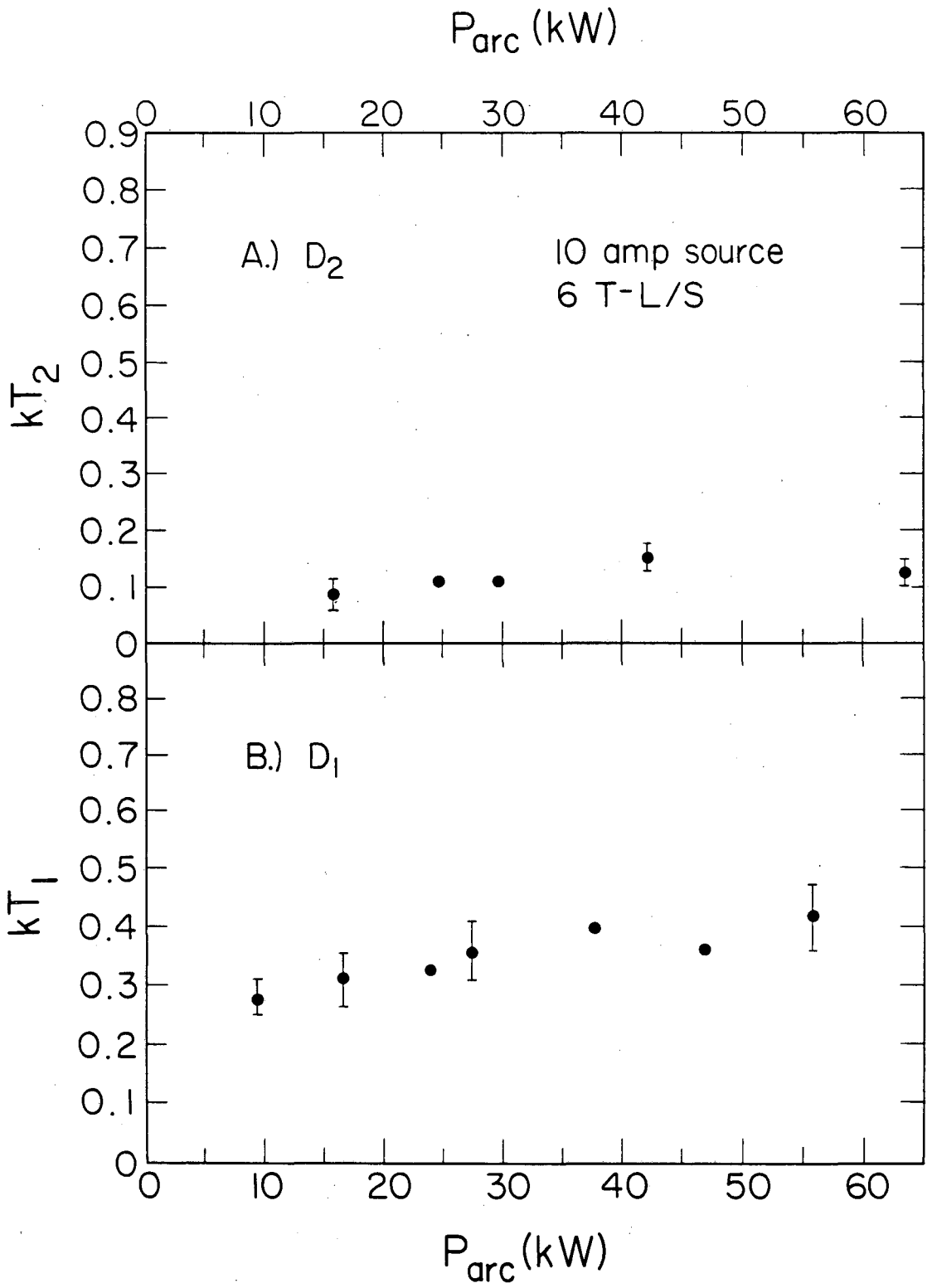

XBL 829-4601

Figure 14

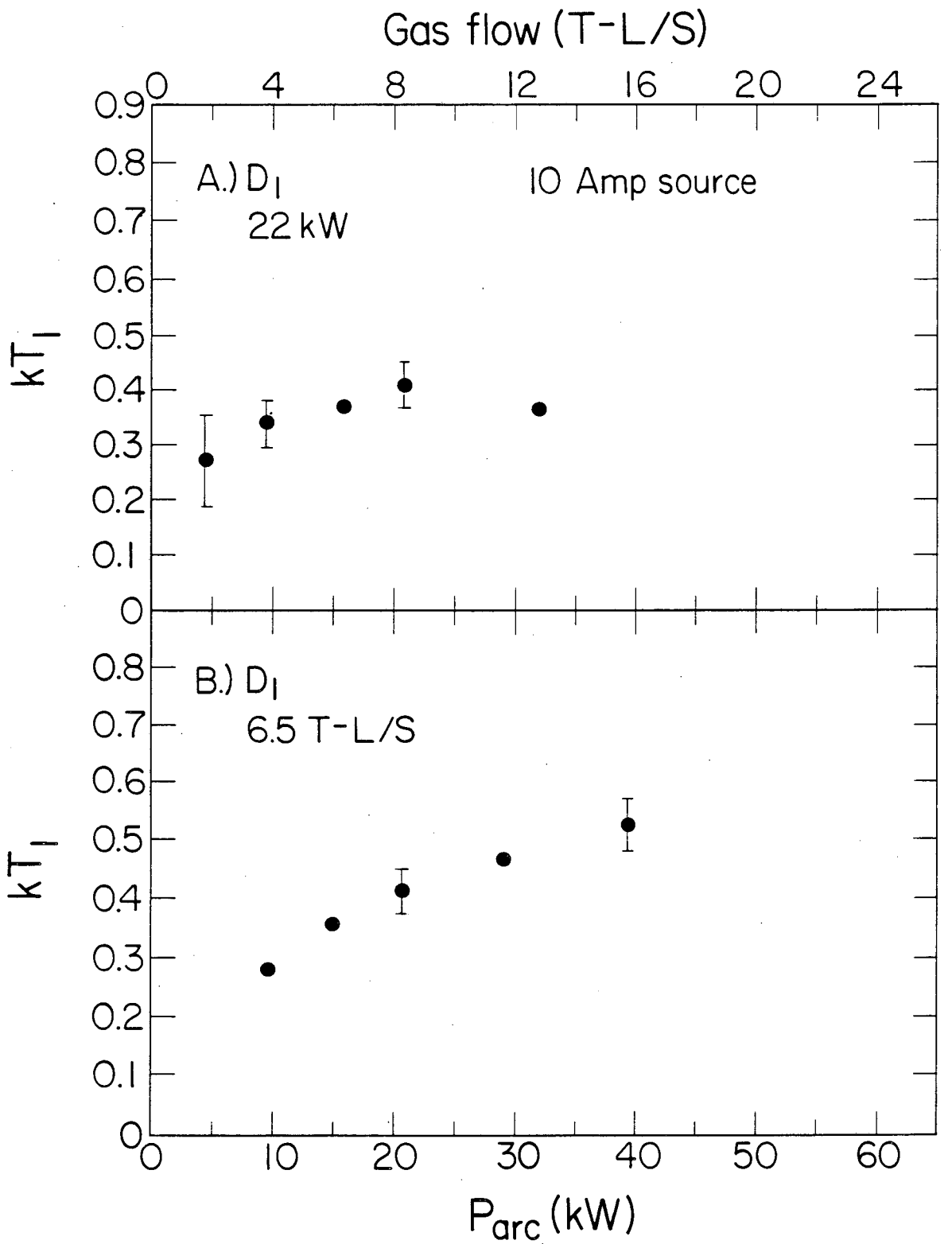

XBL-829-4594

Figure 15

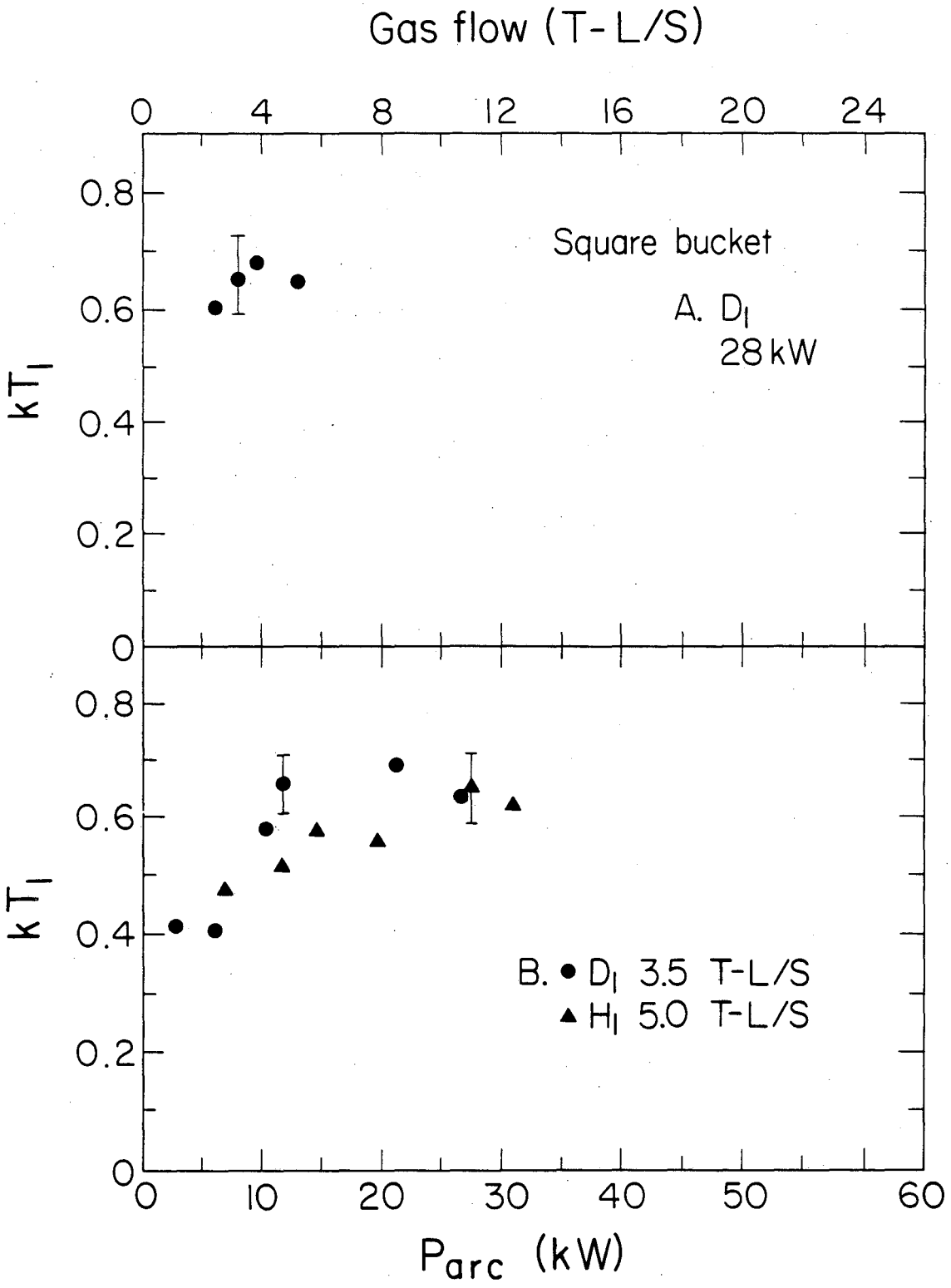

XBL 829-4585

Figure 16

This report was done with support from the Department of Energy. Any conclusions or opinions expressed in this report represent solely those of the author(s) and not necessarily those of The Regents of the University of California, the Lawrence Berkeley Laboratory or the Department of Energy.

Reference to a company or product name does not imply approval or recommendation of the product by the University of California or the U.S. Department of Energy to the exclusion of others that may be suitable.

TECHNICAL INFORMATION DEPARTMENT
LAWRENCE BERKELEY LABORATORY
UNIVERSITY OF CALIFORNIA
BERKELEY, CALIFORNIA 94720